Global and Planetary Change 212 (2022) 103794

Contents lists available at ScienceDirect

Global and Planetary Change

journal homepage: www.elsevier.com/locate/gloplacha

Mercury enrichments of the Pyrenean foreland basins sediments support enhanced volcanism during the Paleocene-Eocene thermal maximum (PETM)

Maxime Tremblin [a,*], Hassan Khozyem [b], Thierry Adatte [c], Jorge E. Spangenberg [d], Charlotte Fillon [e], Arnaud Grauls [f], Teodoro Hunger [a], Andres Nowak [a], Charlotte Läuchli [g], Eric Lasseur [h], Jean-Yves Roig [h], Olivier Serrano [h], Sylvain Calassou [e], François Guillocheau [i], Sébastien Castelltort [a]

[a] Department of Earth Sciences, University of Geneva, Geneva, Switzerland
[b] Department of Geology, Aswan University, Aswan, Egypt
[c] Institute of Earth Sciences, University of Lausanne, Lausanne, Switzerland
[d] Institute of Earth Surface Dynamics, University of Lausanne, Lausanne, Switzerland
[e] TOTAL, Research and Development, Pau, France
[f] Department of Geosciences, TEREGA, Pau, France
[g] Institute of Geological Sciences, Freie Universität Berlin, Berlin, Germany
[h] BRGM (French Geological Survey), Orléans, France
[i] Géosciences Rennes, Université de Rennes 1, Rennes, France

ARTICLE INFO

Keywords:
PETM
Mercury
NAIP
Pyrenees
Source to sink
Climate change

ABSTRACT

The Paleogene records the most prominent global climate change of the Cenozoic Era with a shift from a greenhouse to an icehouse world. Several transient hyperthermal events punctuated this long-term evolution. The most pronounced and the best known of these is the Paleocene-Eocene Thermal Maximum (PETM-56 Ma). This event is associated with global warming, a worldwide perturbation of the carbon cycle, and significant biotic changes. The PETM is primarily recorded by a sharp negative carbon isotope excursion (NCIE) in both carbonates and organic matter of sedimentary successions. The source of the ^{13}C-depleted carbon for the NCIE and whether it was released in one or numerous events is still debated. Several carbon sources have been proposed to explain the PETM-NCIE and the mechanisms that triggered this abrupt climate upheaval. These include, among others, the magmatic and thermogenic release of carbon associated with the emplacement of Large Igneous Provinces (LIP). One proxy for tracking past volcanic emissions in the geological record and testing hypothetical links between volcanism and hyperthermals is the use of mercury (Hg) anomalies found in marine and continental sedimentary successions. Here, we present new high-resolution mercury and stable isotopic records from a continental-marine transect in Pyrenean peripheral basins during the PETM. Compared to deeper marine settings, the significant sedimentation rate that characterizes these high-accommodation and high sediment-supply environments allows the preservation of expanded successions, providing reliable information about the fluctuations of Hg concentration in deposits across the PETM. Our data reveal two large negative carbon excursions across the studied successions. Based on biostratigraphy and the similarity of shape and amplitude of the isotopic excursions with global records, we interpret the largest NCIE as the PETM. This main excursion is preceded by another that we interpret as the Pre-Onset Excursion (POE), found in other profiles worldwide. We find that the POE and the PETM are, in our studied sections, systematically associated with significant Hg anomalies regardless of the depositional environment. These results suggest that large pulses of volcanism, possibly related to the North Atlantic Igneous Province's emplacement, contributed to the onset and possibly also to the long duration of the PETM. Furthermore, the record of higher Hg anomalies in nearshore than offshore settings suggests a massive collapse of terrestrial ecosystems linked to volcanism-driven environmental change triggered

* Corresponding author at: Department of Earth Sciences, University of Geneva, 13 rue des Maraîchers, 1205 Geneva, Switzerland.
E-mail address: maxime.tremblin@unige.ch (M. Tremblin).

https://doi.org/10.1016/j.gloplacha.2022.103794
Received 1 September 2021; Received in revised form 11 February 2022; Accepted 19 March 2022
Available online 24 March 2022

significant Hg loading in shallow marine ecosystems. If this is correct, these findings confirm the primary role of the solid Earth in determining past terrestrial climates.

1. Introduction

The Paleocene-Eocene thermal maximum (PETM) is a major climatic and environmental event that occurred 56 Ma ago (Westerhold et al., 2009). The PETM is characterized by a significant global temperature rise (4–8°C) (Dunkley Jones et al., 2013; Frieling et al., 2017; Sluijs et al., 2011; Zachos et al., 2003) associated with a massive injection of ^{13}C-depleted carbon into the global exogenic carbon reservoirs (Dickens et al., 1995; Zachos et al., 2008) and extensive environmental changes. These include ocean acidification, sea-level rise, an accelerated hydrological cycle, and species migrations and extinctions (e.g., Chen et al., 2018; Cui et al., 2011; Dunkley Jones et al., 2018; Dunkley Jones et al., 2013; Gutjahr et al., 2017; Kirtland Turner, 2018; Kirtland Turner et al., 2017; Kirtland Turner and Ridgwell, 2016; McInerney and Wing, 2011; Schmitz and Pujalte, 2007; Sluijs et al., 2006; Zachos et al., 2003; Zeebe et al., 2016; Zeebe et al., 2009). The massive input of light carbon into the environment is marked by a large negative carbon isotope excursion (NCIE ~3‰ to 6‰) recorded in marine and terrestrial carbonates (e.g., McInerney and Wing, 2011). By providing valuable insight on the link between the carbon cycle, temperature and precipitation variations, and the biotic response to environmental change, the PETM represents a prime geological narrative and concrete perspective of the possible environmental consequences of current and future climate changes (Kirtland Turner, 2018; Stassen, 2016; Zachos et al., 2008; Zeebe et al., 2016; Zeebe et al., 2014).

The shape of the PETM-NCIE, with a rapid 8–23 ky "onset phase" followed by a long 59–113 ky "body phase" characterized by stable and low δ^{13}C values, and a final 42–113 ky-long "recovery phase", distinguishes the PETM from other, more frequent and shorter (~50 ky), astronomically paced Eocene hyperthermal events (Aziz et al., 2008; Murphy et al., 2010; Röhl et al., 2007; Stap et al., 2009; Westerhold et al., 2009; Zeebe et al., 2014). This peculiar NCIE structure is explained by an initial rapid addition of ^{13}C-depleted carbon at the onset of the event, followed by a continuous release across the body and ensuing sequestration (Frieling et al., 2016). However, although the key features of the PETM are well known, the source of the carbon and whether it was released in one or several steps during the "onset phase" remains controversial and is still debated (e.g., Bowen et al., 2015). For a decade, several mechanisms and carbon sources, either alone or combined, have been proposed to explain the PETM-NCIE (e.g., McInerney and Wing, 2011). These include (i) a massive release of methane clathrate (δ^{13}C ~ −60‰) (Dickens et al., 1995) (ii) direct volcanic carbon release (δ^{13}C ~ −6‰) (Gutjahr et al., 2017) and/or thermogenic methane degassing associated with large-scale magmatism in the North Atlantic Igneous Province (NAIP) (Aarnes et al., 2010; Svensen et al., 2010; Svensen et al., 2004), (iii) a release of carbon due to significant wildfires (Kurtz et al., 2003), (iv) the oxidation of organic matter due to the drying of epicontinental seas (δ^{13}C ~ −22‰) (Higgins and Schrag, 2006) or permafrost thawing (δ^{13}C ~ −30‰) (DeConto et al., 2012). Mass balance calculations allow estimating the amount of carbon from each possible source required to account for the observed NCIE. This estimation must be consistent with the observed warming, inferred pCO_2 levels, and carbonate dissolution recorded from sedimentary sequences (McInerney and Wing, 2011). In addition, precise appraisal of the PETM-NCIE magnitude remains challenging because marine carbonates likely underestimate the NCIE while terrestrial carbonates may overestimate it (Bowen and Beerling, 2004; McCarren et al., 2008; McInerney and Wing, 2011). Despite progress, past data-driven reconstructions of the PETM's carbon sources have led to nonunique solutions, and there is currently no agreement on the sources of carbon responsible for its onset and long duration. (Haynes and Hönisch, 2020; Kirtland Turner and Ridgwell, 2016; Kirtland Turner and Ridgwell, 2013; McInerney and Wing, 2011). Furthermore, the observation that the warming appears before the onset of the PETM-NCIE reinforces the idea of multiple releases of carbon throughout the Paleocene-Eocene transition. This initial warming could be a positive feedback that triggered back the release of a large amount of ^{13}C-depleted carbon several thousand years after, at the onset of the PETM (Sluijs et al., 2007). From a high-resolution record of the δ^{13}C of terrestrial deposits in the Bighorn Basin (Wyoming, USA), Bowen et al. (2015) reveal the occurrence of two discrete negative δ^{13}C events within the PETM onset. The authors proposed that the older one, the pre-onset excursion (POE), marks the first phase of massive carbon release and suggested that the PETM-NCIE may have been a feedback to the warming generated by the greenhouse gases released during the POE (Bowen et al., 2015).

The emplacement of a large igneous province (LIP) such as the NAIP may generate multiple and prolonged releases of carbon and could explain both warming and carbonate dissolution associated with the PETM (e.g., McInerney and Wing, 2011; Berndt et al., 2016; Frieling et al., 2016; Gutjahr et al., 2017; Jones et al., 2019a; Jones et al., 2019b; Haynes and Hönisch, 2020). Mass extinctions and rapid climate change seem to be closely correlated with the formation age of LIPs in Earth history, and a causal connection was often proposed between these events (Bergquist, 2017; Bond and Wignall, 2014; Courtillot and Renne, 2003; Ernst, 2014a; Racki, 2020; Rampino and Stothers, 1988; Wignall, 2005). The NAIP is an extended LIP, characterized by the voluminous and rapid emplacement of magma into the shallow crust and the surface, which occurred in two main pulses. The second and more voluminous pulse coincided with the opening of the North Atlantic and began around 56 Ma ago (Abdelmalak et al., 2019; Abdelmalak et al., 2016; Ernst, 2014b; Jones et al., 2019a; Storey et al., 2007a; Wilkinson et al., 2017). Nevertheless, quantification of volcanism in sedimentary archives remains a challenge, and the link between NAIP and PETM remains controversial (Bond and Wignall, 2014; Storey et al., 2007b; Thomas and Bralower, 2005). Limited geochronological data are available for this event, and few measurable LIP products are preserved and could be used as potential marker horizons. However, the few data available show that flood basalt volcanism associated with the opening of the North Atlantic is correlative with the PETM (Wotzlaw et al., 2012).

One alternative method to investigate the possible link between the establishment of the NAIP and the perturbation associated with the PETM is to study mercury (Hg) concentration records in marine and continental sedimentary successions. Volcanism is a significant source of mercury in the atmosphere and ocean (Pyle and Mather, 2003). The relatively long atmospheric residence time of gaseous elemental mercury Hg^0 (0.5 to 2 years) allows global distribution of this element before it gets deposited in sediments (Blum et al., 2014; Percival et al., 2018; Pyle and Mather, 2003; Schroeder and Munthe, 1998; Slemr et al., 1985). Volcanogenic Hg is removed from the atmosphere through oxidation and forms reactive Hg^{2+} soluble in water and prone to be deposited onto land and water by rainfall. Hg may also be deposited directly onto soil or taken up by plant foliage (Ericksen et al., 2003; Fleck et al., 1999; Frescholtz et al., 2003; Grasby et al., 2019). In the ocean, Hg is transferred either by atmospheric deposition (~70%) or by riverine runoff of Hg bound to terrestrial materials (~30%) (Amos et al., 2014). The majority of Hg transported by riverine particles is deposited at oceanic margins, and only a comparatively small amount of this Hg of riverine origin reaches the open ocean (Amos et al., 2014). Ultimately, mercury may also be emitted directly into the ocean through subaqueous volcanism and mid-ocean ridge activity (Bagnato et al., 2017; Bowman et al., 2015; Lamborg et al., 2006). However, in submarine LIP

events, Hg distribution to sedimentary basins may be less extensive because of longer ocean mixing times (Jones et al., 2019a; Percival et al., 2018; Scaife et al., 2017). In modern sediments, a strong correlation between Hg and total organic carbon (TOC) is observed because mercury is principally deposited in sediments adsorbed onto organic Hg-rich complexes (Benoit et al., 1999; Bergquist, 2017; Gehrke et al., 2009; Outridge et al., 2007; Sanei et al., 2012; Stern et al., 2009). As a result, Hg concentrations usually need to be normalized to TOC to determine whether the Hg spikes reflect increased organic matter sequestration or increased Hg fluxes from volcanic emission (Grasby et al., 2019; Sanei et al., 2012). Furthermore, Hg-sulfides complexes formation, as well as absorption of Hg onto iron sulfide minerals (e.g., pyrite (FeS_2)), can host large amounts of Hg in euxinic facies (Bergquist, 2017; Bower et al., 2008; Han et al., 2014; Shen et al., 2020; Shen et al., 2019a). In addition, clay minerals can also absorb Hg, leading to a potential relationship between Hg and Al in environments where phyllosilicate runoff is significant (Bergquist, 2017; Jin and Liebezeit, 2013; Kongchum et al., 2011; Shen et al., 2020; Sial et al., 2016; Sial et al., 2013). This affinity of Hg for clays minerals can lead to a significant terrestrial Hg contribution to shallow marine sediments (Them et al., 2019). Despite these uncertainties, numerous studies have used anomalous peaks in Hg and Hg/TOC ratios preserved in sedimentary successions as an indication of significant volcanic activity and hence have highlighted a possible link between significant environmental perturbations and LIP eruptions (Charbonnier et al., 2017; Charbonnier and Föllmi, 2017; Font et al., 2016; Grasby et al., 2016; Grasby et al., 2013; Jones et al., 2017; Keller et al., 2020; Keller et al., 2018; Percival et al., 2017; Percival et al., 2015; Racki et al., 2018; Sanei et al., 2012; Shen et al., 2019b; Sial et al., 2013; Them et al., 2019; Thibodeau et al., 2016; Thibodeau and Bergquist, 2017). Indeed, the emplacement of LIPs exerts an essential control on the global Hg cycle because of the large-scale effusive and explosive volcanism associated with these events and also because of the activation of hydrothermal vent complexes releasing gases generated by contact metamorphism between intrusive and organic-rich sediments (Aarnes et al., 2015; Aarnes et al., 2010; Heimdal et al., 2019; Jones et al., 2019b; Jones et al., 2019a; Percival et al., 2020; Shen et al., 2019b; Svensen et al., 2004). In the case of the NAIP, only a few studies have provided a continuous record of Hg concentration across the PETM (Jones et al., 2019b; Keller et al., 2018; Kender et al., 2021; Liu et al., 2019). This limited amount of data hampers the identification of the potential causal links between NAIP formation, the perturbation of the carbon cycle, and environmental changes during the PETM.

In the present work, we propose to use Hg concentration in sediments as a tracer of volcanic activity, in association with classical stable isotope composition of carbon and oxygen, Rock-Eval Pyrolysis, and mineralogical analyses to test the possibility of enhanced NAIP activity across the PETM interval. To do this, we focus on Paleocene-Eocene sediments from different sections in peripheral basins of the Pyrenean orogen, encompassing continental to bathyal depositional environments. Previous studies of the PETM have concentrated mainly on deep-sea sites, and in comparison, relatively few continental and shallow marine sections have been studied (Bowen et al., 2015; Koch et al., 1995; Li et al., 2020; Schmitz and Pujalte, 2003; Self-Trail et al., 2017; Stassen et al., 2009; Zamagni et al., 2012). Although studies on deep-sea carbonates provide reliable data on global perturbations associated with the PETM (McInerney and Wing, 2011; Stassen, 2016), they nevertheless may give only a partial record because of the widespread dissolution of deep carbonates associated with the release of carbon during such hyperthermal (McCarren et al., 2008; Zachos et al., 2005). Moreover, such dissolution adds complexity when trying to understand the sequence of carbon-release events. By contrast, continental and shallow-marine areas in tectonic settings with high accommodation and high accumulation rates may offer expanded records of mercury evolution and carbon cycle perturbations during the PETM but may also suffer from significant lithological variability and correlation issues typical of foreland basins. Thus, in addition to potentially recording an expanded PETM-NCIE signal, this work may provide new stratigraphic constraints that allow the correlation between continental, shallow marine, and deep-water successions of the Pyrenean domain during the Paleocene-Eocene epoch.

2. Study sites

The four sites investigated in this study are located on the Pyrenean domain. This sector represented an *E*-W elongated marine gulf throughout the early Paleogene that opened westward into the Bay of Biscay. This gulf was characterized by a central deep-water trough surrounded by shallow-shelf areas to the South, East, and North, in turn, limited by subaerial alluvial plains (Baceta et al., 2011; Plaziat, 1981; Pujalte et al., 2015; Pujalte et al., 2014). Three of the study sections come from well-known field outcrops of Basque (Zumaia) and Tremp basins (Esplugafreda and Serraduy) in the southern Pyrenees (Spain). The last one (Lussagnet) is a drill core through the Paleocene-Eocene interval from the Aquitaine basin in the northern Pyrenees (France) (Fig. 1). These sections were selected as they represent different ranges of facies during the early Paleogene and offer the potential to evaluate how significant climatic disturbances associated with the PETM are recorded through a continental to marine transect. Lithologic successions and the sampling of each site are described in turn.

2.1. Lussagnet (France)

The Lussagnet section consists of a 133 m-thick core (LUG-101, courtesy of TEREGA) located in the Aquitaine Basin, Northern Pyrenees, France (043°46′4″N, 000°13′12″W) (Fig. 1). The facies succession of the section can be subdivided into two main formations (Fm) (Fig. 2). The lower one includes 44 m of dolomitic limestones characteristic of an inner platform setting (950–906 m). The second formation consists of 90 m of wackestone to packstone limestones generally enriched in benthic foraminifera (906–816 m). Few intervals with lacustrine levels that contain charophytes, gastropods, and crustacean cuticles have been identified in this second formation. The larger one of these lacustrine intervals is located between 857 and 844 m. Some detrital inputs (sands and clays) can also occasionally disrupt this carbonate succession. This thick shallow marine to lacustrine sequence represents the northern part of the large carbonate platform surrounding the Bay of Biscay's marine gulf during the beginning of the Paleogene (Fig. 1). Biostratigraphic analyses based on the distribution of large benthic foraminifera and nanoplanktonic fauna allow determining the relative ages of the stratigraphic succession. Thus, the interval between 930.8 and 867.95 m is marked in its upper part by the first significant occurrence of *Fasciculites tympaniformis*, which marks the NP6/NP9 zone (Paleocene). The interval between 864.4 and 894.53 m is attributed to the SBZ3-2 biozones due to the presence of *Thalmannita Madrugaensis, Cookinolina* cf. *rajkae*, at the base (894.53–885.85 m), and *Cribrobulimina carniolica*, *Dictyoconus turriculus*, and *Fallotella alavensis* at the top (866.95–867.95 m). All these arguments allow us to attribute a late Paleocene age to sediments between 930 and 864 m. The presence of taxa such as *Orbitolites gracilis* (824.18–839.2 m, SBZ5-6), *Alveolina ellipsoidalis* (829.72 m, SBZ6), *Alveolina avellana avellana* (831.15 m, SBZ5), and the genus *Orbitolites* up to 543.35 m allow to attribute the interval 824.18 to 843.35 m to the SBZ6-5 biozones and thus to the Lower Eocene. The exact stratigraphic position of the PETM remains uncertain due to the absence of reliable biostratigraphic markers in the interval where this event is suspected of occurring (864–843.35 m). In this crucial interval, the only significant presence is *Idalina sindjarica* (860.83 m), a taxon whose distribution covers the SBZ6 to SBZ3 biozones. Two brecciated and finely karstified intervals (loferitic facies) disturb the stratigraphic succession. The first occurred at the limit between the dolomitic and the calcitic limestones at the end of the Thanetian (905–906 m). The second took place between 857 and 860 m deep within the foraminifera limestone formation and before the lacustrine deposits. Because of a possible substantial

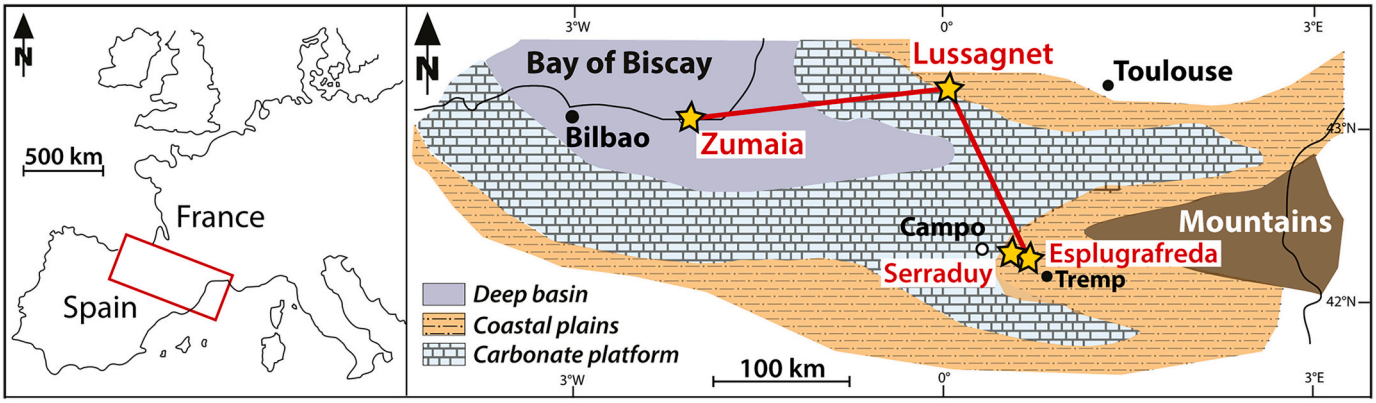

Fig. 1. Situation and map of the study area with the main depositional palaeoenvironments during the PETM (Modified after Pujalte et al., 2014).

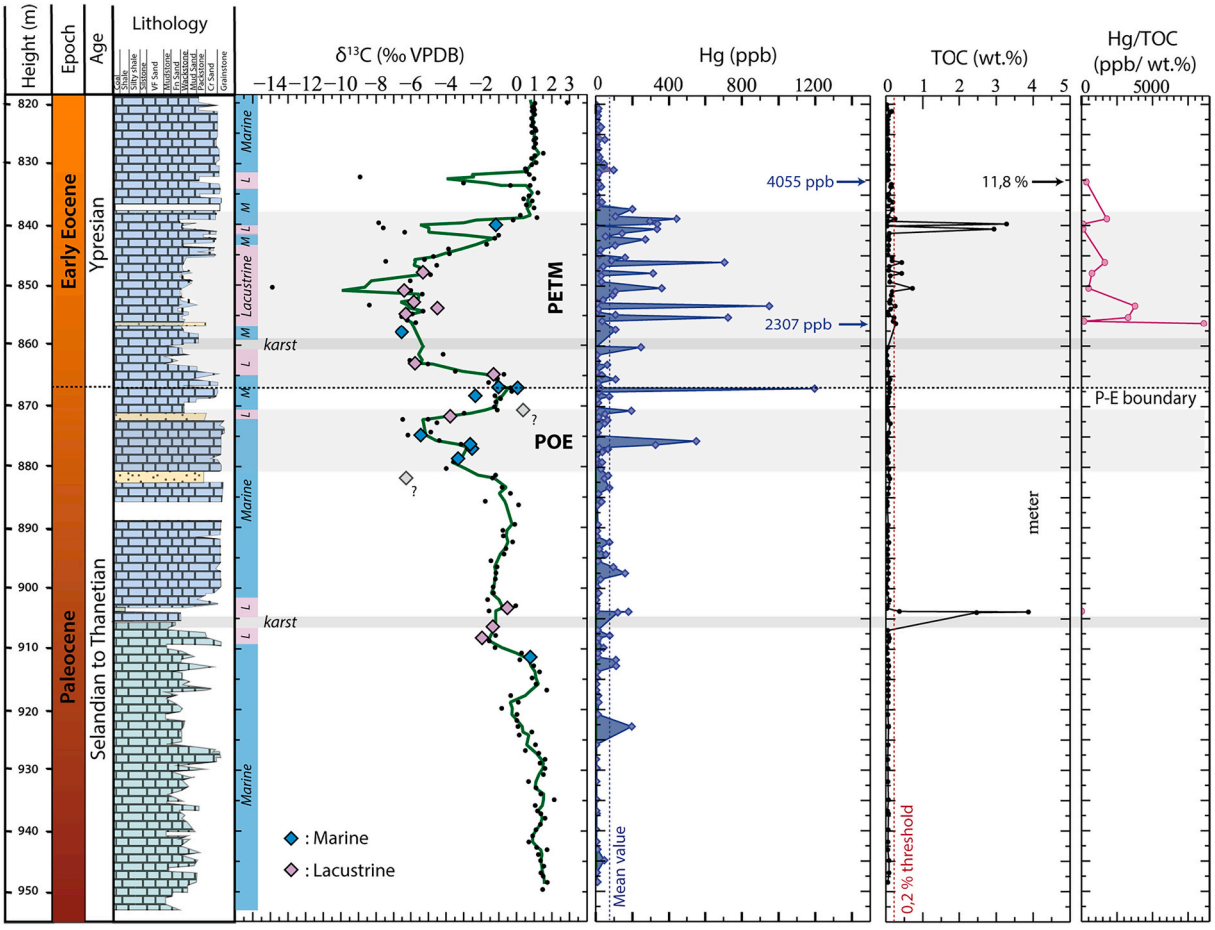

Fig. 2. Stratigraphic log, $\delta^{13}C$ (‰), mercury (Hg, ppb) and Hg/TOC (ppb/wt%), and total organic carbon (TOC, wt%) data of the Lussagnet section (France). $\delta^{13}C_{whole\text{-}rock}$ are shown with black points and $\delta^{13}C_{matrix}$ with diamond (Light-blue for marine samples and in pink for lacustrine samples). Grey diamonds represent samples associated with a significant proportion of sandstone. This heterogeneity in the sediment could arise for a larger variability in the carbon isotopic signal. Because of this peculiar lithology, these points were excluded from the study. The green curve represents 3-points $\delta^{13}C$ moving average. Dark-grey shaded bands mark karstic/brecciated levels observed. The grey shaded area shows the location of the POE-NCIE and PETM-NCIE. The red dashed line in the TOC graph shows the recommended threshold for TOC concentrations to report Hg/TOC values (Grasby et al., 2016). The blue dashed line in the Hg graph denotes the background mean value for the site. (For interpretation of the references to color in this figure legend, the reader is referred to the web version of this article.)

alteration of the primary signal, these two intervals characteristic of emersion were excluded from our study. Samples were generally collected at a 1-m interval over the 218 m of the section and with a higher resolution (~ 0.5 m) through the suspected PETM interval (881–840 m).

2.2. *Esplugafreda (Spain)*

The Esplugafreda section is located ~330 km to the East of the Basque Basin, South-Central Pyrenees, Spain, east of Aren (042°14′50″N, 000°45′13″E) (Fig. 1). This section represents the eastern margin of the Eocene marine paleo-basin. The Esplugafreda section is a

300 m thick continental section that spans the Paleocene and Early Eocene interval of the Tremp Group. This succession is subdivided into several formations precisely described by Schmitz and Pujalte (2003, 2007), but only the upper two: the Esplugafreda and Claret Formations, span the PETM interval (Fig. 3). The Esplugafreda Fm consists of a red silty mudstone-dominated alluvial succession with intercalated channelized calcarenites and calcareous conglomerates (Dreyer, 1993). The red mudstone contains abundant calcareous nodules 2–5 cm in diameter. At the base of the Claret Fm stands an incised valley fill (IVF) which erodes the red mudstones for 15 m. This IVF is overlapped by an extended conglomerate sheet known as the Claret Conglomerate (CC), which is interpreted as a mega-fan formed at the onset of the PETM (Schmitz and Pujalte, 2007). The CC is itself overlain by some tens of meters of paleosoils of the Claret Fm and, finally, by marine Ilerdian limestones that mark the flooding of the sector by the sea after the PETM (Pujalte et al., 2014). The 187 samples used here cover the last 100 m of the Esplugafreda Fm, cross the CC and the PETM interval, and continue 46 m through the Claret Fm.

2.3. Serraduy (Spain)

The Serraduy section is located in the Tremp Basin, approximately 12 km westward from Esplugafreda (042°19′25″N, 000°34′20″E) (Fig. 1). This section can be therefore considered as a western equivalent of the Esplugafreda section. However, the Esplugafreda section is strictly continental during the Thanetian, whereas this more distal section records interfingering between the continental Esplugafreda Fm and the coeval marine carbonates. The studied section here spans the upper part of the Esplugafreda Fm and the Claret Fm previously described for the Esplugafreda section. At Serraduy, the Esplugafreda Fm consists of red mudstones with well-developed soil horizons rich in calcareous nodules intercalated with upper Thanetian marine carbonates (TH1 and TH2) (Fig. 4). The Claret Fm is bounded at the base by a prominent erosional surface and by the presence of the Claret Conglomerate, itself is overlain by yellowish soils which are accumulated during the “onset” and the “body” of the PETM (Pujalte et al., 2014). As seen in Esplugafreda, the upper part of the Claret Fm is overlain by the marine Ilerdian limestone (Domingo et al., 2009; Pujalte et al., 2014). Sixty-three samples were

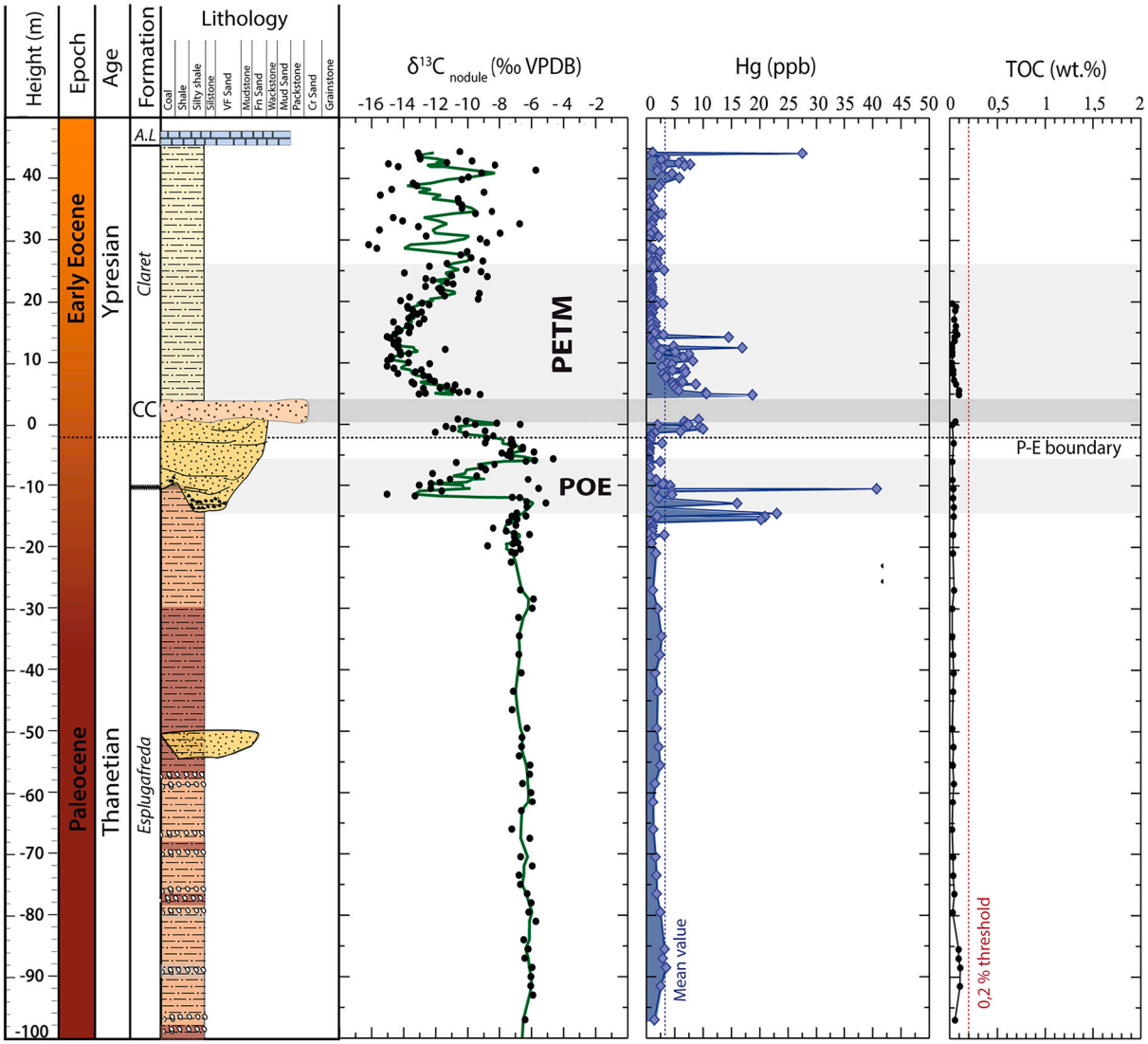

Fig. 3. Stratigraphic log, $\delta^{13}C$ (‰), mercury (Hg, ppb), and total organic carbon (TOC, wt%) data of the Esplugafreda section (Spain). The green curve represents 3-points $\delta^{13}C$ moving average. The grey shaded area shows the approximate position of the POE-NCIE and PETM-NCIE. A dark-grey shaded band marks the stratigraphic position of the Claret conglomerate. The red dashed line in the TOC graph shows the recommended threshold for TOC concentrations to report Hg/TOC values (Grasby et al., 2016). The blue dashed line in the Hg graph denotes the background mean value for the site. (AL: Alveolina limestone, CC: Claret conglomerate). (For interpretation of the references to color in this figure legend, the reader is referred to the web version of this article.)

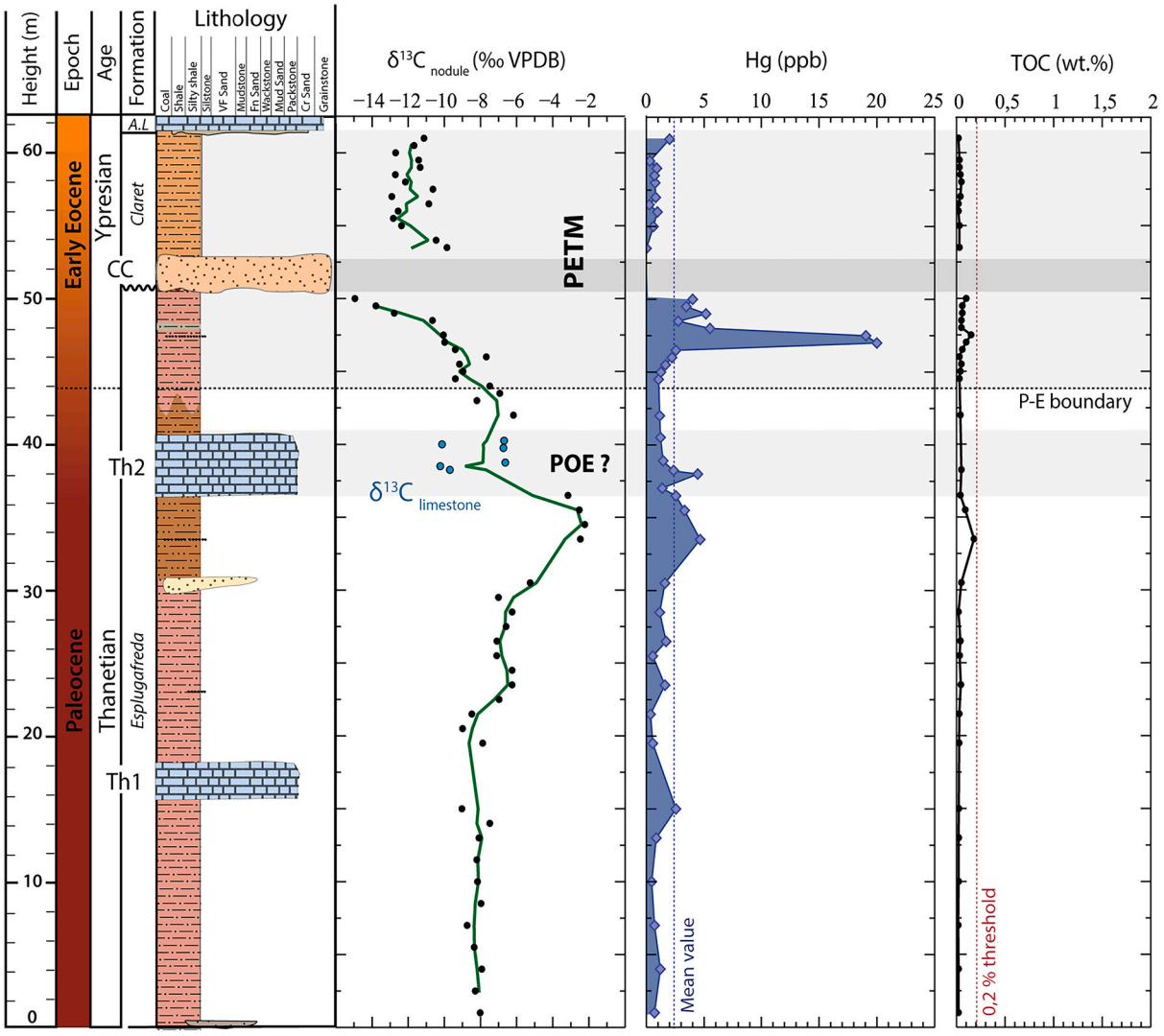

Fig. 4. Stratigraphic log, $\delta^{13}C$ (‰), mercury (Hg, ppb), and total organic carbon (TOC, wt%) data of the Serraduy section (Spain). The $\delta^{13}C_{nodule}$ are shown with black points and $\delta^{13}C_{whole\text{-}rock\ carbonate}$ are shown with light-blue points. Green curve represents 3-points $\delta^{13}C$ moving average. The grey shaded area shows the approximate position of the POE-NCIE and PETM-NCIE. A grey shaded band marks the stratigraphic position of the Claret conglomerate. The red dashed line in the TOC graph shows the recommended threshold for TOC concentrations to report Hg/TOC values (Grasby et al., 2016). The blue dashed line in the Hg graph indicates the background mean value for the site. (AL: Alveolina limestone, CC: Claret conglomerate, TH1: Lower Thanetian limestone, TH2: upper Thanetian limestone). (For interpretation of the references to color in this figure legend, the reader is referred to the web version of this article.)

collected with a resolution sampling varying from 1.5 to 0.5 m across the Paleocene-Eocene transition.

2.4. Zumaia (Spain)

The Zumaia section is located in the Basque Country, North-Eastern Spain, at the Itzurun beachfront of the town of Zumaia (043°18′4.5″ N, 002°15′31.2″ W) (Fig. 1). This section represents the distal member, at middle-lower bathyal paleo-depths (~ 1000 m), of the Esplugafreda and Serraduy sections (Pujalte et al., 2015). This section consists of a thick "siliciclastic unit" (SU) occurring within an alternation of marls and marly limestones, with intercalated thin-bedded turbidites (Fig. 5). The SU is ascribed to the PETM based on biostratigraphically constrained isotopic profiles of whole-rock carbonate samples (Schmitz et al., 1997) and dispersed organic carbon (Storme et al., 2012). The Zumaia section is one of the classic PETM localities and is the subject of numerous studies (Alegret et al., 2018; Canudo et al., 1995; Dunkley Jones et al., 2018; Schmitz et al., 1997; Storme et al., 2012). The high-resolution whole-rock carbonate isotope analysis allows a detailed stratigraphic correlation to other key deep-ocean and terrestrial PETM reference sections, providing a robust temporal framework for this event (Dunkley Jones et al., 2018). Here the zero-reference point is taken at the top of the prominent limestone bed, located ~0.3 m below the base of the "siliciclastic unit" and corresponds to the one proposed by Dunkley Jones et al. (2018). A total of 80 samples were collected for this study, and complete data of Dunkley Jones et al. (2018). The samples used here cover the PETM interval and begin ~3.5 m below the beginning of the siliciclastic unit and continue ~1 m above.

3. Materials and methods

Carbon and oxygen isotope analysis ($\delta^{13}C$ and $\delta^{18}O$ values) were performed on whole-rock samples for the marine section of Lussagnet and Zumaia. Complementary to the whole rock analyses, 26 pure carbonate matrix samples were separated by micro-drilling of the Lussagnet cored plugs on the stratigraphic interval where the PETM is suspected to occur (882–840 m) and where minor brecciated levels are abundant. This micro-sampling excluded veins and open-space filling calcite,

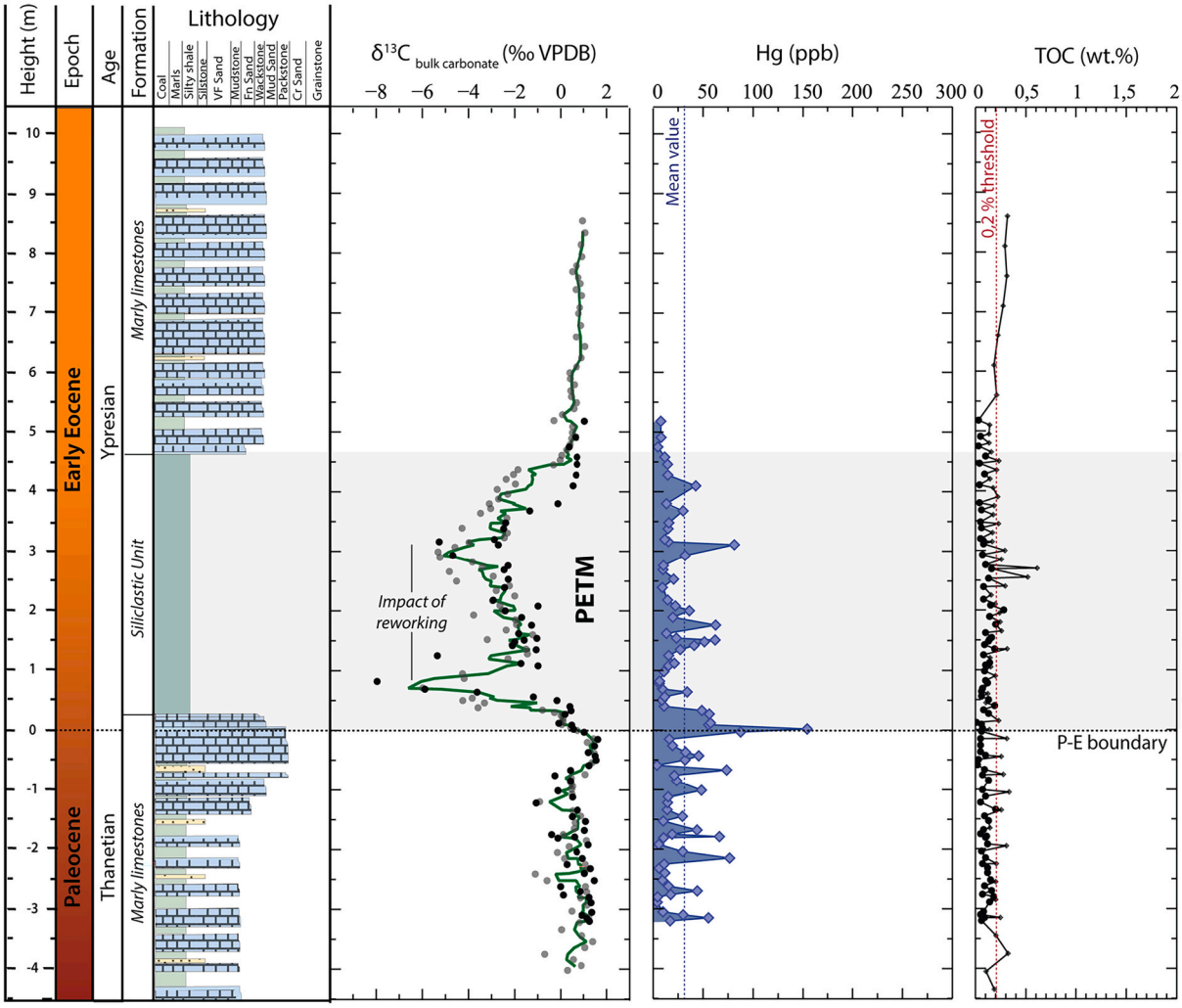

Fig. 5. Stratigraphic log, $\delta^{13}C$ (‰) (black points: data from this study; grey points: data from Dunkley Jones et al., 2018), mercury (Hg, ppb), and total organic carbon (TOC, wt%) data of the Zumaia section (Spain). Green curve represents 3-points $\delta^{13}C$ moving average. The grey shaded area shows the approximate position of the PETM-NCIE. The red dashed line in the TOC graph shows the recommended threshold for TOC concentrations to report Hg/TOC values (Grasby et al., 2016). The blue dashed line in the Hg graph denotes the background mean value for the site. (For interpretation of the references to color in this figure legend, the reader is referred to the web version of this article.)

brecciated zones, and bioclasts and allowed to compare the $\delta^{13}C$ and $\delta^{18}O$ records from whole-rock samples with those from the drilled matrix materials. For the continental sections (Serraduy and Esplugafreda), isotope profiles are based on in situ soil carbonate nodules. The carbonate nodules were sieved from the bulk paleosol material and then cleaned by repeated washes with deionized water. The whole-rock samples and the carbonate nodules were crushed and powdered in an agate mortar. The sample powders were analyzed for their stable carbon and oxygen isotope compositions at the University of Lausanne (Switzerland) using a Thermo Fisher Scientific (Bremen, Germany) Gas Bench II carbonate preparation device connected to a Thermo Fisher Delta Plus XL isotope ratio mass spectrometer. The carbon and oxygen isotope compositions are reported in the delta (δ) notation as the per mil (‰) isotope ratio variations relative to the Vienna Pee Dee Belemnite standard (VPDB). The analytical reproducibility estimated from replicate analyses of the international calcite standard NBS-19 and the laboratory standard Carrara marble was better than ±0.05‰ (1σ) for $\delta^{13}C$ and ± 0.1‰ (1σ) for $\delta^{18}O$.

The Hg concentration measurements and Rock-Eval Pyrolysis were performed on the same set of whole-rock samples analyzed for carbon and oxygen isotopes. Hg contents were determined at the University of Lausanne (Switzerland) using a Zeeman R-915F (Lumex, St. Petersburg, Russia) high-frequency atomic absorption spectrometer set at Mode 1 (700°C). The samples were analyzed in duplicates, and a certified external standard (Chinese alluvium GSD-11, 72.0 ± 9 ppb Hg; Zintwana et al., 2012) was used for calibration purposes (r = 0.99, for measured vs. certified values) and to guarantee the analytical quality.

The total organic carbon (TOC) contents were determined using a Rock-Eval 6 at the University of Lausanne (Switzerland), the pyrolysis effluents (mostly hydrocarbons) were detected and quantified with flame ionization detection, and CO and CO_2 were quantified by infrared detection. The analytical uncertainty was ±0.14%.

Major (ME) and Trace Element (TE) were determined by X-ray fluorescence spectrometry (XRF, PANalytical PW2400 spectrometer, University of Lausanne, Switzerland) of pressed discs of powdered samples and Mowiol II polyvinyl alcohol. The major element (MEs) results are reported in weight percent and the trace elements (TEs) in parts per million (ppm). Analytical reproducibility monitored by replicate analyses of selected samples was lower than ±5% for MEs and TEs. Analysis accuracy was assessed using international and in-house standard reference materials (TS1-Cement, TS3-Clay, TS4-Limestone, TS5-Marlstone, TS7-Sandstone, 372-Portland cement, 368-Dolomite). The detailed paleoenvironmental interpretation of the MEs and TEs is beyond the scope of the present paper. The elemental contents were

analyzed in this study only to evaluate the dependence of Hg according to anoxia and/or clay content. TEs were analyzed in 76 samples of Lussagnet through the suspected PETM interval. MEs and TEs were determined throughout the entire section at Zumaia (80 samples).

Whole-rock was analyzed at the University of Lausanne (Switzerland) by X-Ray Diffraction (XRD), using a Thermo Scientific ARL X-TRA diffractometer. The whole-rock mineralogy was determined by a semi-quantitative method, using XRD peak intensities of the main minerals compared to external standards (Adatte et al., 1996; Klug and Alexander, 1974; Kübler, 1983). The whole-rock mineralogy was analyzed in 26 samples of Lussagnet through the suspected PETM interval.

4. Results

The results of the stable isotope and Rock-Eval analyses of the different studied sections are shown in Figs. 2–5, and the complete dataset is available as electronic Supplementary Information (**Supplemental Tables A.1–4**). The TOC contents were generally <0.2 wt%, i.e., below the threshold value for reporting reliable Hg/TOC ratios (Grasby et al., 2016).

4.1. Lussagnet (France)

The $\delta^{13}C$ values of whole-rock carbonates in the Lussagnet profile vary between −2‰ and 2‰ during the first 65 m of the section (Fig. 2). A first negative $\delta^{13}C$ excursion from ~0‰ to −5‰ is observed between 886 and 869 m. This NCIE corresponds to the POE previously identified in terrestrial settings (Bowen et al., 2015) and several shallow-marine environments (Li et al., 2020; Self-Trail et al., 2012; Zamagni et al., 2012). A second and larger NCIE, interpreted as the PETM onset, is recorded between 867 and 862 m, with values shifting from −1‰ to −6‰. This NCIE is maintained up to 846 m, with mean values of −6.2‰. This body phase is followed by a progressive recovery to pre-PETM and POE values at 839 m depth (Fig. 2). The micro-drilled unaltered matrix samples show similar results as whole-rock samples. The $\delta^{13}C$ values recorded in the matrix samples mimic the global evolution of the whole-rock $\delta^{13}C$ curve, showing two NCIEs of similar amplitudes (~ −5‰ for the PETM-NCIE). The similarity between these two signals confirms that the whole-rock carbonate $\delta^{13}C$ record corresponds to a primary signal and can be safely used for paleoenvironmental interpretation.

Before the POE, the Hg concentrations at Lussagnet show a steady evolution with values ranging between 2 and 50 ppb and few spikes reaching 110 to 197 ppm. A first anomalous Hg spike of 551 ppm occurs at 875.7 m during the POE, and then Hg concentrations return to background values. A total of 15 Hg spikes (93–949 ppb) are present in the PETM interval reaching a maximum value of 2307 ppm in the core of the NCIE. After the PETM, Hg contents return to background values and stay stable until the top of the section (Fig. 2). An exceptionally high Hg anomaly (4055 ppb) is present at 832.81 m. The TOC contents are stable with generally low values (< 0.7 wt%). Only 12 of the 139 samples analyzed for quantifying the TOC content show values >0.2 wt%, the recommended threshold for interpreting the Hg/TOC values, and 10 of them are associated with Hg anomalies (>300 ppb). The Hg/TOC values recorded for these 10 samples are high (Fig. 2) and superior to the global Hg/TOC mean value (71.9 ppb/wt%) derived from the compilation of all Hg/TOC values available in the bibliography (Grasby et al., 2019). Thus the persistence of the anomaly in Hg/TOC ratios in these sediments suggests that these Hg spikes do not reflect increased organic matter sequestration.

4.2. Esplugafreda (Spain)

At Esplugafreda, the $\delta^{13}C$ values of pedogenic carbonate nodules show a relatively stable trend throughout the Esplugafreda Formation with values between −5.1‰ and −8.8‰ (Fig. 3). A first NCIE (~ −8‰) is observed at the transition between the Esplugafreda Formation and the Claret Formation, followed by a return to values around −7‰ (Fig. 3). This excursion is interpreted as the record of the POE at Esplugafreda. This first NCIE immediately preceded a second prominent NCIE with values reaching −15‰ after the CC deposit in the Claret Formation (Fig. 3). Based on the stratigraphic position and paleontological studies of the nearby Campo section (Orue-Etxebarria et al., 2001; Schmitz and Pujalte, 2003), this second significant negative shift in $\delta^{13}C$ is attributed to the PETM. The $\delta^{13}C$ values begin to gradually increase toward pre-PETM values approximately 10 m after the CC. However, they show a large variability on the last 18 m of the Claret Formation, challenging the unambiguous identification of the end of the recovery phase (Fig. 3).

The Hg concentrations are generally low and vary between 0 and 5 ppb throughout the section, with a mean value of 3.3 ppb. This long-term trend is disturbed by two changes (Fig. 3). The first one occurs during the POE with values between 16 and 41 ppb; the second one occurs during the onset and the body of the PETM with values up to 20 ppb (mean value of 6.5 ppb). A final spike of 27.5 ppb Hg is recorded at the top of the section and end of the Claret Formation. The TOC remains stable throughout the entire section, with mean values of 0.1 wt% (Fig. 3).

4.3. Serraduy (Spain)

The $\delta^{13}C$ evolution of the Serraduy section shows the same trend as those established at Esplugafreda, with values between −5‰ and −9‰. The $\delta^{13}C$ values rise between 33 m and 37 m to a maximum of −2.2‰ before shifting toward more negative values, reaching −10.2‰ in the Thanetian carbonates (between 38 and 40.3 m) (Fig. 4). This first excursion is similar in amplitude to the one observed in Esplugafreda (~ −7‰) and could be here interpreted as the POE record. However, because this excursion is also correlated to a significant lithological change (Fig. 4), it is difficult to attribute this excursion to the POE univocally. The major NCIE, which corresponds to the PETM, is observed a few centimeters below the CC with values reaching a minimum of −15‰. The PETM-NCIE onset seems to occur few meters before the CC, which was not the case in Esplugafreda. Above the conglomerate, the $\delta^{13}C$ values remain relatively stable with a mean value of −11.7‰ until the Ilerdian carbonate base (Fig. 4). The onset of the PETM-NCIE can be therefore clearly determined at Serraduy, but the identification of the body and recovery phases of the NCIE remains difficult.

The Hg concentrations are low throughout the section, averaging 2.5 ppb. During the POE interval, a small Hg spike of 4,5 ppb is recorded. The more significant Hg anomaly occurred during the onset of the PETM, with Hg concentrations reaching 20 ppb (Fig. 4). The TOC values are extremely low and remain stable throughout the entire section with values between 0.05 wt% and 0.2 wt% and are not correlated with any significant Hg concentration change (Fig. 4).

4.4. Zumaia (Spain)

The $\delta^{13}C$ composition of whole-rock carbonates across the Zumaia section shows a relatively stable trend in the 5 m below the Siliclastic Unit (SU) with values typically ranging from −1‰ to 1.6‰. The $\delta^{13}C$ values drop to around −8‰ just before the SU and stay low (0.7‰ to −5.4‰) through this lithological unit (Fig. 5). Above this, the $\delta^{13}C$ values vary between −0.7‰ and 1‰ up to the end of the section. These new results are consistent with previous studies of the Zumaia section, which attributed this NCIE to the PETM (Dunkley Jones et al., 2018; Schmitz et al., 1997). Based on the $\delta^{13}C$ profile, we define the onset of the PETM-NCIE at 0 m, a few centimeters before the beginning of the SU (Fig. 5). During the body of the NCIE, the $\delta^{13}C$ are higher values and diverge from the typical PETM-NCIE signal. This shift to pre-excursion values is attributed to a relative increase of reworked material, shown

by the presence of Cretaceous nannofossils (Dunkley Jones et al., 2018). Consequently, it is not easy to precisely define the end of the NCIE body and the start of the recovery period.

Hg concentrations in Zumaia are highly variable during the Thanetian, with values in the 3.7–76.5 ppb range (Fig. 5). A Hg anomaly phase with values between 48.7 and 154.1 ppb is noticed 30 cm before the SU and coincides with the beginning of the PETM onset. During the body/recovery phase of the PETM, the Hg contents return to lower values. They generally remain stable, having only four spikes of values higher than the background average (27.3 ppb) for this section (Fig. 5). The TOC contents vary between 0.01 wt% and 0.28 wt%. No significant TOC variations were observed in this section (Fig. 5).

5. Discussion

The record of two distinct NCIEs within the PETM interval and their association in the studied sections with significant Hg concentration anomalies is the most striking feature of our high-resolution data set. The studied sites display a wide range of Hg concentrations and $\delta^{13}C$ values showing a similar global trend. These variations are correlated with changes in depositional environments observed along a continental to oceanic transect. The deep-sea and shallow marine to lacustrine sediments show globally higher $\delta^{13}C$ values and Hg concentrations spikes, and smaller NCIEs. In comparison, pedogenic carbonates from continental sediments show lower $\delta^{13}C$ values and Hg anomalies but record higher NCIEs (Fig. 6). Several processes linked with each studied environment may have lead to differences in the record of Hg and $\delta^{13}C$ values. Therefore, these processes must be considered before interpreting the geochemical signal as an indicator of the global environmental perturbation associated with the PETM.

5.1. Identification of the PETM in the Pyrenean peripheral basins

5.1.1. The carbon isotope records along a continental to oceanic transect

The sharp drop in $\delta^{13}C$ values associated with the PETM is global and, therefore, often used as a correlative tool when limited biostratigraphic data are available, particularly in continental sections (Koch et al., 1992). The $\delta^{13}C$ signal reported here is used to assess the occurrence of the PETM across the Pyrenean domain and assign a relative age to the associated Hg anomalies recorded along the studied successions.

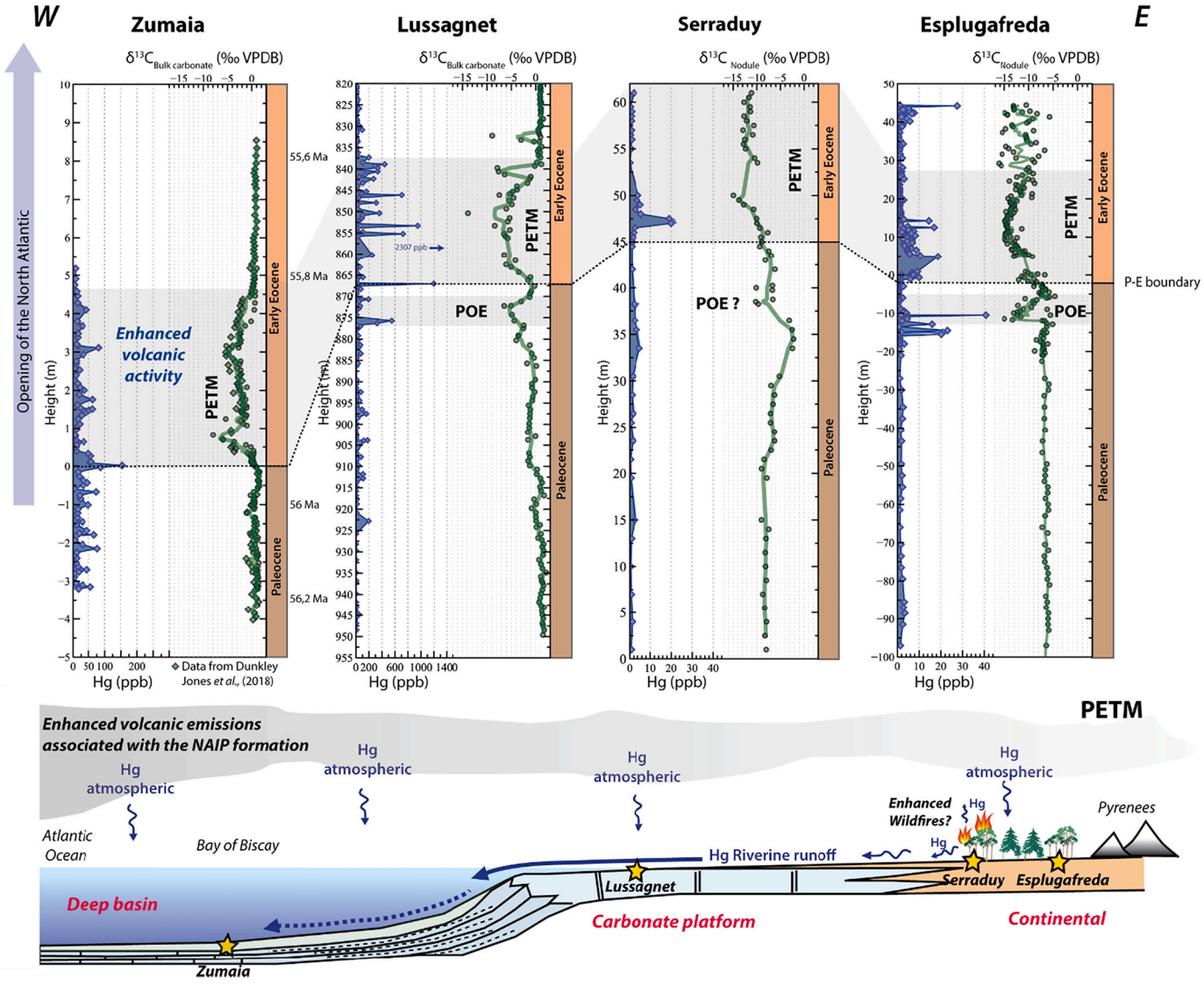

Fig. 6. Pyrenean record of the environmental disturbances associated with the enhancement of the volcanism across the PETM. Significant perturbations of the carbon and mercury cycles are recorded whatever the environment considered during the POE and the PETM. The amplitude of both the Hg anomalies and the NCIEs is correlated with the type of depositional environment. The rate and amount of mercury accumulation in sediment vary from the continent to the ocean leading to a wide variation in mercury anomalies.

The dataset shown in this work comes from different depositional environments. The geochemical signals were derived from whole-rock carbonates in the marine sections and from soil nodule carbonates in the continental ones. Components and processes determining the ^{13}C content and the relative contributions of the various reservoirs may explain the differences in the $\delta^{13}C$ values and NCIE amplitudes. The compilation of data from different environments shows a wide range of $\delta^{13}C$ records and NCIEs associated with the PETM (McInerney and Wing, 2011). In the oceanic realm, the primary $\delta^{13}C$ values of whole-rock carbonates vary mainly with changes in concentration and $\delta^{13}C$ of marine dissolved inorganic carbon (DIC) and the fraction of carbon deposited on the ocean floor as carbonate or organic matter. An abrupt release of ^{13}C-depleted organic carbon results in a decrease of $\delta^{13}C_{DIC}$, which is ultimately reflected in the $\delta^{13}C$ of the whole-rock carbonate (Cramer et al., 2003). The $\delta^{13}C$ values of pedogenic carbonate nodules vary with the soil properties, atmospheric pCO_2 values, carbon input rate, soil organic matter content, and soil respiration rate (Bowen et al., 2015; Bowen et al., 2004; Cerling, 1984; Honegger et al., 2019; Jolivet and Boulvais, 2020; Sheldon and Tabor, 2009). During the PETM, marine carbonates were often subjected to seafloor dissolution and bioturbation by deep-sea organisms that could attenuate the amplitude of the excursion (McCarren et al., 2008; McInerney and Wing, 2011; Zachos et al., 2005). In the continent, the buildup of tropospheric humidity associated with the PETM wet climate enhanced the carbon cycling through terrestrial ecosystems (i.e., increased plant productivity, soil CO_2 content, and soil organic matter), leading to an amplification of the NCIE in pedogenic carbonate nodules (Bowen et al., 2004). Low-amplitude NCIEs are thus generally found in deep marine environments, intermediate NCIEs in shallower environments, and more significant NCIEs in continental environments (McInerney and Wing, 2011). Earth system models were thus developed to estimate the true magnitude of the global carbon isotope excursion associated with the event providing a framework for interpreting PETM records (Kirtland Turner and Ridgwell, 2016; Kirtland Turner and Ridgwell, 2013). These models suggest that the amplification of terrestrial and surface ocean NCIEs could also be consistent with a rapid carbon release rate without invoking additional factors that could artificially enhance the apparent NCIEs in terrestrial proxies or dampen the NCIEs in marine proxies (Kirtland Turner and Ridgwell, 2016). Nevertheless, even if the excursion size varies widely between different depositional settings, the record of the NCIEs from a wide variety of marine and terrestrial sources confirms that the perturbation of the carbon cycle is global and can be recorded throughout a continental to oceanic transect.

A relative sea-level drop was registered throughout the Pyrenean basin during the late Paleocene and the early Eocene (Pujalte et al., 2014). It may have caused changes in the depositional environment of the studied sedimentary successions. In turn, the sea-level changes may have led to variations in the $\delta^{13}C$ values, independently of any significant global environmental disturbance. Additionally, possible diagenetic processes may have altered the primary $\delta^{13}C$ records, particularly in shallow shelf carbonates where the influx of meteoritic waters can be significant (Godet et al., 2016). These post-depositional processes can bring further complexity to the correlation of continental and open-marine stable isotope records. A close examination of possible depositional environment changes throughout the successions studied and a cross-plot of $\delta^{13}C$ versus $\delta^{18}O$ was realized for each site (**Supplemental Fig. A.1**) to test the robustness of our carbon signal during the suspected POE and PETM intervals. The reliability of the carbon signals recorded for each site is discussed in turn in the following sections.

5.1.2. Carbon isotope signal from the shallow water carbonate of Lussagnet

The magnitude of the whole-rock PETM-NCIE (~ −5‰) of the Lussagnet carbonate platform (Fig. 2) is higher and relatively more negative (i.e., more ^{13}C-depleted carbonates) than North America continental shelf (−2.8‰ to −3.5‰) (John et al., 2008; Self-Trail et al., 2017; Self-Trail et al., 2012) but is comparable to values reported for shallow carbonate platform and lacustrine carbonate section of the southern Pyrenees (−6‰) (Li et al., 2021) and of a Central and Himalayan Tethys section (−3‰ to −7‰) (Li et al., 2020; Zhang et al., 2020). As previously reported in these studies, the NCIE-POE is particularly well characterized in shallow-water environments. At Lussagnet, the occurrence of a significant 10 m thick negative spike (~ 4‰) just before the onset of the PETM stands as evidence of this first perturbation of the carbon exogenic pool (Fig. 2). Several factors may have a strong influence on the $\delta^{13}C$ values recorded in carbonate ramps or platforms. For instance, the restriction in the carbon reservoir size of the platform-top water mass, the change of the local carbon weathering fluxes from land, the early diagenesis of carbonate mudstone in organic-rich sediments, and/or sea-level change can lead to relative ^{13}C depletion in platform carbonates (Colombié et al., 2011; Immenhauser et al., 2002; Li et al., 2020; Patterson and Walter, 1994; Swart, 2008). Some observations allow us to exclude some of these processes as controls on the $\delta^{13}C$ variations observed at Lussagnet.

During the end of Paleocene and Early Eocene, the carbonate platform of Lussagnet was connected west toward the ocean, and the corresponding sedimentary succession was deposited during a long-term transgressive sequence. Therefore, the $\delta^{13}C$ values reported here were not strongly influenced by restricted water mass or carbon weathering fluxes from land. The late Paleocene to early Eocene carbonate strata where the NCIEs occurred is dominated mainly by calcium carbonate with high $\delta^{18}O$ values. The cross-plot of the $\delta^{13}C$ and $\delta^{18}O$ values show no significant correlation, and the $\delta^{13}C$ shifts reported are not correlated to $\delta^{18}O$ variations (r^2 = 0,03 during the suspected PETM interval; **Supplemental Fig. A.1**). This lack of $\delta^{13}C$-$\delta^{18}O$ covariations suggests that a substantial post-depositional (diagenetic) alteration of the primary $\delta^{13}C$ values is unlikely. Sea-level change can also shift the $\delta^{13}C$ trend record on the carbonate platform toward more positive or negative values (Swart, 2008). For instance, a deepening of the depositional environment can lead to a more significant influence of deeper-water carbonate and hence can shift the $\delta^{13}C$ toward lower values. However, at Lussagnet, the NCIEs are not related to a drowning of the platform. Instead, the onset of the NCIE coincides with a relative sea-level fall. This relative sea-level change, possibly related to local tectonic uplift during ongoing Pyrenean formation or tectono-magmatic activity in the North Atlantic, is well established on the southern side of the platform in the Tremp-Graus and Ager Basin (Li et al., 2021; Minelli et al., 2013; Pujalte et al., 2014). At Lussagnet, this sea-level change is recorded by the occurrence of subaerial exposure surfaces (905–906 m and 857–960 m) at the end of the PETM "onset" and by lithologic swings between innermost carbonate ramp facies and fluvio-lacustrine depositional setting during the PETM "body" (Fig. 2). Lacustrine carbonates are generally ^{13}C depleted compared to marine carbonates. In general, the carbon isotope composition of authigenic lacustrine carbonates is mainly controlled by the isotopic composition of the DIC of inflowing waters, the CO_2 exchange between lake water and the atmosphere, and the balance between primary and secondary productivity and respiration in the lake (Leng and Marshall, 2004). Groundwaters and river waters that recharge the lakes have $\delta^{13}C_{DIC}$ values typically low because a significant proportion of the CO_2 comes from organic matter oxidation (e.g., plant and soil respiration). This phenomenon associated with the photosynthesis/respiration of aquatic plants in the lake explains the negative $\delta^{13}C$ values of lake carbonates. It cannot be excluded that significantly ^{13}C-depleted carbonates (−14‰ to −8‰) reported at Lussagnet during the body of the NCIE (Fig. 2) could be in part due to the occurrence of fluvio-lacustrine intervals and thus are probably not correlated to an extensive input of carbon in the atmospheric-oceanic system. However, PETM-NCIE onset with a clear shift from −1.1‰ to −6.1‰ occurred a few meters before the interval characterized by the deposition of lacustrine carbonates. Moreover, this shift toward more negative $\delta^{13}C$ values is recorded both through the lacustrine and marine facies (Fig. 2) Finally, the recovery phase with a gradual shift toward more positive values (−1‰ to 0‰) occurred during a transgressive trend

establishing in a fully marine environment (Fig. 2). Furthermore, the isotopic signal recorded at Lussagnet is consistent with the evolution of $\delta^{13}C$ recorded in the southern part of the carbonate platform at Campo in the southern Pyrenees (Li et al., 2021). We conclude that despite a possible disturbance of the signal associated with depositional environment change during the "body phase" of the PETM, the carbon isotopic evolution obtained at Lussagnet records the global disturbance in biogeochemical cycles through the PETM and can be used as a chemostratigraphic tool to support both regional and global correlation.

5.1.3. Carbon isotopic signal from the continental sections of Esplugafreda and Serraduy

The $\delta^{13}C$ continental record of Esplugafreda and Serraduy represents typical values for soil carbonate nodules from the Paleocene (Bowen et al., 2015; Bowen et al., 2002; Bowen et al., 2001; Honegger et al., 2019), with an average value of −7.1‰ and −6.8‰, respectively (Fig. 3). The $\delta^{18}O$ values show a relatively stable trend throughout the sections (**Supplemental Tables A.2–3**). Oxygen and carbon isotopes are not coupled during the PETM in the continental record, as already observed by Schmitz and Pujalte (2003) and Bowen et al. (2001). However, this stable trend in the oxygen values argues for limited burial diagenesis in these sections. Moreover, the cross-plot of the $\delta^{13}C$ and $\delta^{18}O$ values show poor to moderate correlations ($r^2 = 0,42$ during the suspected PETM interval for Esplugfreda, $r^2 = 0,18$ during the suspected PETM interval for Serraduy; **Supplemental Fig. A.1**), suggesting that the significant shifts in $\delta^{13}C$ values are not diagenetic artifacts. The new data reported here significantly increase the resolution of the $\delta^{13}C$ record (Schmitz and Pujalte, 2003) through the interval preceding the PETM at Esplugafreda and pinpoint the stratigraphic position of the POE for this reference sites of the Tremp-Graus basin. Additionally, this data set confirms the existence of a temporal lag between the onset of the PETM and the Claret conglomerate (CC) deposition throughout the sediment routing system of the Tremp-Graus basin (Duller et al., 2019). The CC was deposited during the PETM onset phase at Esplugafreda and at its end for the slightly more distal site of Serraduy. The PETM-NCIE (−7‰) magnitude reported at Esplugafreda and Serraduy is similar as previously observed in other soil nodule profiles in Wyoming and China (Bowen et al., 2015; Bowen et al., 2002; Bowen et al., 2001). The negative $\delta^{13}C$ shift that characterizes the POE at Esplugafreda is recorded in an interval without significant facies changes (Fig. 3). Conversely, the NCIE-POE of Serraduy corresponds to an apparent lithological change (Fig. 4). Pre- and post-POE $\delta^{13}C$ values were carried on soil carbonate nodule. In contrast, POE $\delta^{13}C$ values come from bulk carbonate limestone measurement, meaning that a lithological effect on the signal cannot be excluded entirely. Moreover, in comparison to the Lussagnet and Esplugafreda signal, no recovery phase is observed in the $\delta^{13}C$ for this site. On the other hand, the $\delta^{13}C$ limestone values recorded here are ^{13}C-depleted in comparison to classical values recorded on the carbonate ramp during the end of the Paleocene (Li et al., 2020; Self-Trail et al., 2012; Zamagni et al., 2012) and are comparable to the $\delta^{13}C$-POE values reported at Lussagnet. However, additional work is needed to confirm the presence of the NCIE-POE at Serraduy. For instance, because the NCIE-POE is linked with Hg anomalies in the other study sites, a higher resolution record of Hg anomalies across the Thanetian marine limestone (TH2; Fig. 4) would help to identify whether or not this interval corresponds to the POE.

5.1.4. Carbon isotope signal from the deep-sea section of Zumaia

The deep-water section of Zumaia represents one of the most complete and representative sections of the Paleocene to Eocene hemipelagic succession of the Pyrenees and provides a robust PETM temporal framework (Dunkley Jones et al., 2018; Storme et al., 2012). The high-resolution whole-rock carbonate isotope signal reported here is consistent with previous studies of the Zumaia section (Dunkley Jones et al., 2018; Schmitz et al., 1997) but differs markedly from the other studied Pyrenean sections in that there is only one NCIE occurring within the stratigraphic succession (Fig. 5). The POE recorded at each other's locality is missing. Although some negative $\delta^{13}C$ shifts in the marls and limestone couplets of the latest Paleocene immediately underlie the large NCIE, these changes and the absolutes values recorded are within background variations. Moreover, dissolution and dilution processes that occurred just above and during the PETM resulted in very low $CaCO_3$% contents across this interval (Dunkley Jones et al., 2018). Correlating univocally, one of the pre-PETM negative $\delta^{13}C$ shifts to the POE is rather difficult.

5.2. Pyrenean mercury anomalies reflect enhanced volcanism throughout the PETM

Our high-resolution carbonate ^{13}C data compilation allows us to pinpoint the stratigraphic position of the PETM and the POE throughout the Pyrenean domain (Fig. 6). Although site-specific constraints prevent the use of the $\delta^{13}C$ variations for mass balances calculations, the signal obtained across the ocean-continent transect allows the correlation between the recorded Hg anomalies and the observed NCIEs. While volcanism is the primary source of Hg in the environment, several other processes could cause a significant release and accumulation of Hg. They should therefore be carefully considered before interpreting Hg anomalies in sedimentary rocks.

5.2.1. Non-volcanic causes of mercury enrichment in sediments

Sedimentary mercury can be hosted in various sediment fractions, including organic matter (Benoit et al., 1999; Bergquist, 2017; Gehrke et al., 2009; Outridge et al., 2007; Sanei et al., 2012; Stern et al., 2009), sulfides (Bergquist, 2017; Bower et al., 2008; Han et al., 2014; Shen et al., 2019a, 2020) and, more rarely, clay minerals (Shen et al., 2020; Sial et al., 2013). Based on analogy to modern oxic marine sediments, organic matter is commonly assumed to be the dominant host phase in ancient sediments (e.g., Grasby et al., 2019; Shen et al., 2020). The assumption of an organic host phase is correct in mainly cases, but assuming such a relationship without specific evidence could be risky (Shen et al., 2020). Indeed, if Hg complex readily with organic matter under oxic conditions, under intensely sulfidic conditions, Hg-sulfide complexes dominate. Moreover, in a shallow-marine environment, it was demonstrated that clay minerals could be the dominant host phases (Kalvoda et al., 2019; Percival et al., 2018; Shen et al., 2019c). In order to explore the possible influence of these processes on the Hg variations, trace and major element abundances were determined in Lussagnet and Zumaia sections. The Lussagnet section was selected because this site recorded the more significant Hg anomalies during the PETM interval, and the Zumaia section was selected because the PETM interval corresponds to the deposition of the "siliciclastic unit" that marks an increase of runoff due to significant changes in regional hydrology (Dunkley Jones et al., 2018). In these two sections, the correlation between change in Al and Zr contents and Hg concentrations is poor (**Supplemental Figs. A.2–3**), indicating that the Hg fluctuations recorded in these sites are not controlled primarily by changes in clay content, even if some Hg is probably adsorbed into clay. If the occurrence of euxinic levels in the oxidized red and yellow soils of Esplugafreda and Serraduy is unlikely, the occurrence of euxinic levels in the marine environments of Lussagnet and Zumaia can not be totally excluded. The poor correlation between Hg and selected redox-sensitive TEs (e.g., V, Mo, U, Ni) (**Supplemental Figs. A.2–3)** at Lussagnet and Zumaia suggest that most of the Hg anomalies observed in this study are not linked to Hg-sulfides complexes formation under anoxic conditions. This observation is also supported by the fact that the different Hg peaks (Hg > 100 ppb) observed at Lussagnet do not correspond to pyrite-rich levels (**Supplemental Table A.1)**. Taking together these results suggests that even clay minerals and Hg-sulfide complexes may host Hg, the organic fraction represent probably the primary host for Hg in the sediments of the various study sites.

Because Hg concentrations are often directly linked to TOC contents,

the mercury concentration is classically normalized by the TOC contents before interpreting the Hg anomalies as derived from the volcanism activity. The low TOC values, below the measurement uncertainties (< 0.2%), recorded in all studied sections, hamper the classical use of the Hg/TOC (Figs. 2–5). However, this extremely low TOC content reported in the four studied sections and the fact that no significant correlation is observed between Hg concentration and TOC content suggest (**Supplemental Tables A.1–4)** that Hg peaks are not linked to an increase of organic matter scavenging. At Lussagnet, only one abrupt spike in Hg concentration (4055 ppb) is correlated with a substantial increase of the TOC content (11.8 wt%) (Fig. 2 **and Supplemental Table A.1**). Since this sample contains a significant amount of coal, it is difficult to univocally discriminate the contribution of volcanism and/or Hg scavenging by organic matter. Thus, even if the influence of volcanism cannot be excluded for the significantly higher Hg deposition in this coal sample, we decided to exclude this point of our study. Permafrost thawing can release Hg (DeConto et al., 2012; Schuster et al., 2018), thus increasing its environmental concentration. However, the late Paleocene is characterized by a greenhouse climate state with both poles ice-free and much higher temperatures than present days for high latitudes (Pagani et al., 2014). The existence of large permafrost reserves under these climatic conditions is thus unlikely.

5.2.2. *Site-specific uncertainties on mercury sequestration*

On a global basis, the Hg anomalies observed in the Pyrenean foreland basins is correlative with similar anomalies reported on continental shelf sections located around the NAIP during the Paleocene-Eocene transition (Jones et al., 2019b; Keller et al., 2018; Kender et al., 2021)), albeit with considerable variability in magnitude among sections (Fig. 6). The deep marine Zumaia section shows Hg anomalies between 50 and 150 ppb, whereas the continental sections of Esplugafreda and Serraduy exhibit anomalies between 10 and 45 ppb. In comparison, the carbonate platform of Lussagnet displays extreme spikes, reaching 2307 ppb Hg. These results indicate that proximity to the continent substantially impacts the amount of Hg deposited in the sediments (Fig. 6). Indeed, the Hg is derived mainly from direct atmospheric fallout in deep oceanic sites. In continental settings, volcanogenic Hg is deposited onto land by rainfall directly onto soil or is taken up by plant foliage. In comparison, in shallow-marine environments, the Hg can be concentrated in the sediment from both direct volcanic sources (via atmospheric deposition) and remobilization of Hg from other terrestrial reservoirs (e.g., soil erosion and biomass burning) (Shen et al., 2022). Thus, even if the initial source of exogenous Hg is volcanic, Hg can be ultimately hosted and redistributed during its transport within intermediate reservoirs (Blum et al., 2014; Them et al., 2019). This observation is in line with the compilation of NCIE and Hg Toarcian data, which revealed a significant correlation between the proximity of the site to the landmass and the recorded Hg anomalies (Them et al., 2019). Nearshore environments consistently record higher mercury anomalies released from the remobilization of terrestrial sediments than deep oceanic sites which are dominated by a direct atmospheric fallout (Them et al., 2019). Across our transect, the nearshore marine section of Lussagnet is hence more likely to preserve Hg cycle perturbations to a greater extent than the other sites. For instance, modern wildfires produce widespread fly ash that can increase the supply of Hg to soils and surface waters (Burke et al., 2010), and a similar relationship was previously suggested for proximal Hg anomalies during the latest Permian extinction (Grasby et al., 2017). The massive wildfires likely related to climatic feedback associated with volcanism could have triggered increased soil erosion because of the vegetation destruction. This could rise the Hg loading in the nearshore environments of Lussagnet, challenging the identification of the primary source (s) of sedimentary Hg. Thus, although if no traces of coal ash were observed in the study sites, an indirect influence of these processes in the mercury contents cannot be excluded, and the extremely high Hg concentrations recorded at Lussagnet (Fig. 2) probably reflect a mixing input from volcanic sources (via direct atmospheric deposition) and terrestrial sources (via volcanism-related increases in continental erosion and runoff). Despite these complexities, Hg enrichments coincide in all the depositional environments (Fig. 6) from deep basin to terrestrial environment, reflecting a global mercury loading through the Paleocene-Eocene transition. This close concordance between Hg enrichments and carbon cycle perturbations probably implies a common source. Thus, we suggest that the Hg anomalies observed throughout the Pyrenean domain are likely associated with the environmental destabilization associated with enhanced volcanism during the POE and the PETM intervals.

5.3. *NAIP volcanism as a cause of the PETM*

The late Paleocene to early Eocene period coincides with the establishment of the North Atlantic Igneous Province (NAIP) (Storey et al., 2007a; Wilkinson et al., 2017). The NAIP is one of the most important ancient Large Igneous Province (LIP) known (Ernst, 2014a), with a volume of igneous material estimated to reach 5.10^6 to 10.10^6 km^3 (Eldholm and Thomas, 1993; Holbrook et al., 2001). The main bulk of the NAIP volcanism erupted in two phases. The first phase began at c. 62–57 Ma, and the second phase coinciding with continental rifting volcanism occurred at c. 56–54 Ma (Storey et al., 2007a; Ernst, 2014a; Ernst, 2014b; Wilkinson et al., 2017). This second phase of the NAIP formation produced enormous volumes of basaltic magma and closely coincided with the PETM. This volcanism linked with the opening of the North Atlantic may thus have triggered the PETM (Berndt et al., 2016; Gutjahr et al., 2017; Jones et al., 2019a; Storey et al., 2007a; Svensen et al., 2004). NAIP volcanism may generate such a perturbation in global carbon and mercury cycles. Indeed, several mechanisms associated with the NAIP may have released a significant amount of mercury and ^{13}C-depleted carbon to the atmosphere-ocean system. NAIP magma could release carbon dioxide (Eldholm and Thomas, 1993), while explosive volcanism can affect the global Hg cycle. Thermogenic methane, carbon dioxide (Svensen et al., 2004), and mercury (Jones et al., 2019b; Percival et al., 2018; Shen et al., 2019b) were also produced by thermal maturation of organic material within carbon-rich basins due to igneous sills. These gases may migrate to the seafloor in hydrothermal vent complexes in sufficient volumes to trigger the environmental change associated with the PETM (Berndt et al., 2016; Frieling et al., 2016). However, because it is difficult to find measurable LIP products such as tephra layers in geological archives, providing a strict causal relationship between the NAIP and the PETM remains complicated (Jones, 2015). The supposed connection between intense NAIP volcanism and the PETM is principally derived from the study of seismic reflection profiles and geochemical and petrographic data from the Norwegian Sea (Aarnes et al., 2015; Svensen et al., 2004). This assumption strongly depends on the timing of sill-intrusions in the organic-rich Vøring and Møre basins. Unfortunately, if large sill intrusions during NAIP formation are likely to be a source of carbon and Hg to the environment, the close temporal coincidence between these intrusions and the PETM remains still debated.

Our data show that significant Hg anomalies stratigraphically coincide with the PETM interval (Fig. 6). These results provide additional independent evidence that volcanic and/or thermogenic eruptions associated with the emplacement of the NAIP have played a crucial role in the PETM climate change. The present high-resolution dataset confirms the existence of one first phase of carbon release just before the PETM. This pre-onset excursion (POE) is recorded at Lussagnet, Serraduy, and Esplugafreda and is associated with significant Hg anomalies in two of our study sites (Fig. 6). This temporal coincidence between the POE-NCIE and Hg anomalies gives new evidence of a significant carbon release predating the PETM. Our results support a volcanic origin for the initial warming observed before the PETM. This carbon-forced warming could represent positive feedback for submarine methane hydrate dissociation at the PETM (Bowen et al., 2015; Secord et al., 2010; Sluijs

et al., 2007; Wieczorek et al., 2013). Multiple Hg anomalies during the "body" of the PETM also attest to the sustained activity of volcanism during the PETM. This observation tends to confirm a volcanic source for the longer-term ^{13}C-depleted carbon release responsible for the long duration of the body of the NCIE. Based on carbon cycle box model, previous studies propose that multiple releases of greenhouse gases from vent complexes could explain the shape of the NCIE, the warming, and the deep ocean carbonate dissolution pattern observed in sedimentary records (Frieling et al., 2016; Zeebe et al., 2009). A recent study proposed that the massive degassing of greenhouse gases throughout the hydrothermal vent complexes can explain the totality of PETM-NCIE excursion without implying another organic-carbon reservoir destabilization (Jones et al., 2019a). However, the precise link between Hg anomalies, NAIP volcanisms, and PETM climate change appears complex. Indeed, significant Hg anomalies are observed during and after the "recovery phase" and confirm that volcanism pulses continued although a CO_2 drawdown (Fig. 6). This difference in behavior between the mercury and carbon systems may be related to changes in the magma production rates and dominant emplacement style (Abdelmalak et al., 2016; Saunders, 2016; Storey et al., 2007b). Thermogenic gas release from contact metamorphism and volcanic eruptions are different processes. The spatial distribution and the magnitude of Hg anomalies from these sources may differ considerably. Thus, it cannot be excluded that Hg anomalies do not always equate to the same level of carbon input to the system (Jones et al., 2019b). For instance, a shift in the dominant mode of emplacement from sill intrusion to surface volcanism during the NCIE could lead to a more worldwide release of Hg without thermogenic ^{13}C-depleted gas into the atmosphere-oceanic system (Jones et al., 2019b). A second hypothesis may also explain the Hg anomalies during the recovery phase without necessarily involving volcanic origin. Indeed, it cannot be ruled out that these anomalies were due to the substantial mercury loading from soil erosion during the "recovery phase". However, because the Hg anomalies stopped at the end of the "recovery phase", we argue that these Hg anomalies are probably due to a change in the dominant mode of volcanism throughout the Paleocene-Eocene transition. This complex relationship between Hg anomalies, NAIP emplacement mode, and PETM-NCIE remains yet poorly understood. Further works need to be done before elucidating the succession of events responsible for the PETM climate change.

6. Conclusions

This study highlights Hg anomalies and carbon isotopic signals across the PETM from four sections spanning a continental-marine transect in Pyrenean foreland basins. Unlike classical deep ocean sites, the high accumulation rate that characterizes these environments allows preservation of mercury and carbon cycle perturbations at high resolution during the Paleocene-Eocene transition. In the studied sections, significant Hg anomalies coincide with the PETM-NCIE. The influences of local processes or changes in TOC and Hg sequestration have been tested and reveal that these anomalies are mainly of volcanic origin. Nonetheless, the wide variation of the magnitude of observed Hg anomalies between localities suggests that the depositional environments may have had important control on the Hg sequestration. Furthermore, the timing of Hg peaks, considered here as proxies of volcanic activity of regional/global significance, coincides with a rise in the NAIP activity. Therefore, this suggests that the NAIP is the source of the Hg anomalies recorded across the Pyrenean domain during the PETM. The record of a pre-onset excursion (POE) associated with mercury anomalies immediately before the PETM also suggests that NAIP magmatism may have initiated a positive carbon cycle feedback leading to the PETM events. This precursor event can trigger an abrupt release of carbon from other temperature-sensitive near-surface reservoirs worldwide. However, evidence for elevated volcanism at the end of the PETM-NCIE highlights the complex relationship between volcanism forcing and climate. A better constrain of these changes may be crucial to understand better the climate feedbacks responsible for the hyperthermal conditions associated with the PETM.

Author contributions

MT wrote the manuscript. MT, SC, TA and JES designed the research, interpreted the data, and interacted on the paper. JES performed isotope analyses. CF, TH, AN, CL, HK, TA, MT and SC collected the field and core data. CF and AG provided access to the Lussagnet core. EL and OS provided Lussagnet previous core description. JYV and SyC provided access to funding through the S2S project. FG contributed to initial data interpretation. All authors reviewed the manuscript.

Declaration of Competing Interest

The authors declare no competing interests.

Acknowledgments

We thank TEREGA for allowing access to the Lussagnet core. This work was funded by the 'Source-to-Sink' project of the CONVERGENCE Total/BRGM program. The authors also thank, Aurélien Virgogne, Daniel Michoux and Guillaume Charbonnier for useful discussions. Finally, we are grateful to J. Shen and an anonymous reviewer for their constructive reviews, which greatly improved this manuscript.

Appendix A. Supplementary data

Supplementary data to this article can be found online at https://doi.org/10.1016/j.gloplacha.2022.103794.

References

Aarnes, I., Svensen, H., Connolly, J.A.D., Podladchikov, Y.Y., 2010. How contact metamorphism can trigger global climate changes: modeling gas generation around igneous sills in sedimentary basins. Geochim. Cosmochim. Acta 74, 7179–7195. https://doi.org/10.1016/j.gca.2010.09.011.

Aarnes, I., Planke, S., Trulsvik, M., Svensen, H., 2015. Contact metamorphism and thermogenic gas generation in the Vøring and Møre basins, offshore Norway, during the Paleocene–Eocene Thermal Maximum. J. Geol. Soc. Lond. 172, 588–598. https://doi.org/10.1144/jgs2014-098.

Abdelmalak, M.M., Meyer, R., Planke, S., Faleide, J.I., Gernigon, L., Frieling, J., Sluijs, A., Reichart, G.-J., Zastrozhnov, D., Theissen-Krah, S., Said, A., Myklebust, R., 2016. Pre-breakup magmatism on the Vøring margin: Insight from new sub-basalt imaging and results from Ocean Drilling Program Hole 642E. Tectonophysics 675, 258–274. https://doi.org/10.1016/j.tecto.2016.02.037.

Abdelmalak, M.M., Planke, S., Polteau, S., Hartz, E.H., Faleide, J.I., Tegner, C., Jerram, D.A., Millett, J.M., Myklebust, R., 2019. Breakup volcanism and plate tectonics in the NW Atlantic. Tectonophysics 760, 267–296. https://doi.org/10.1016/j.tecto.2018.08.002.

Adatte, T., Stinnesbeck, W., Keller, G., 1996. Lithostratigraphic and mineralogic correlations of near K/T boundary clastic sediments in northeastern Mexico: implications for origin and nature of deposition. In: The Cretaceous-Tertiary Event and Other Catastrophes in Earth History. Geological Society of America, pp. 211–226. https://doi.org/10.1130/0-8137-2307-8.211.

Alegret, L., Reolid, M., Vega Pérez, M., 2018. Environmental instability during the latest Paleocene at Zumaia (Basque-Cantabric Basin): the bellwether of the Paleocene-Eocene Thermal maximum. Palaeogeogr. Palaeoclimatol. Palaeoecol. 497, 186–200. https://doi.org/10.1016/j.palaeo.2018.02.018.

Amos, H.M., Jacob, D.J., Kocman, D., Horowitz, H.M., Zhang, Y., Dutkiewicz, S., Horvat, M., Corbitt, E.S., Krabbenhoft, D.P., Sunderland, E.M., 2014. Global biogeochemical implications of mercury discharges from rivers and sediment burial. Environ. Sci. Technol. 48, 9514–9522. https://doi.org/10.1021/es502134t.

Aziz, H.A., Hilgen, F.J., van Luijk, G.M., Sluijs, A., Kraus, M.J., Pares, J.M., Gingerich, P. D., 2008. Astronomical climate control on paleosol stacking patterns in the upper Paleocene–lower Eocene Willwood Formation, Bighorn Basin, Wyoming. Geology 36, 531. https://doi.org/10.1130/G24734A.1.

Baceta, J.I., Pujalte, V., Wright, V.P., Schmitz, B., 2011. Carbonate platform models, sea-level changes and extreme climatic events during the Paleocene-early Eocene greenhouse interval: a basin–platform–coastal plain transect across the southern Pyrenean basin, 28th IAS M. ed. In: Pre-Meeting Field-Trips Guidebook.

Bagnato, E., Oliveri, E., Acquavita, A., Covelli, S., Petranich, E., Barra, M., Italiano, F., Parello, F., Sprovieri, M., 2017. Hydrochemical mercury distribution and air-sea exchange over the submarine hydrothermal vents off-shore Panarea Island (Aeolian arc, Tyrrhenian Sea). Mar. Chem. 194, 63–78. https://doi.org/10.1016/j.marchem.2017.04.003.

Benoit, J.M., Gilmour, C.C., Mason, R.P., Heyes, A., 1999. Sulfide controls on mercury speciation and bioavailability to methylating bacteria in sediment pore waters. Environ. Sci. Technol. 33, 951–957. https://doi.org/10.1021/es9808200.

Bergquist, B.A., 2017. Mercury, volcanism, and mass extinctions. Proc. Natl. Acad. Sci. 114, 8675–8677. https://doi.org/10.1073/pnas.1709070114.

Berndt, C., Hensen, C., Mortera-Gutierrez, C., Sarkar, S., Geilert, S., Schmidt, M., Liebetrau, V., Kipfer, R., Scholz, F., Doll, M., Muff, S., Karstens, J., Planke, S., Petersen, S., Böttner, C., Chi, W.-C., Moser, M., Behrendt, R., Fiskal, A., Lever, M.A., Su, C.-C., Deng, L., Brennwald, M.S., Lizarralde, D., 2016. Rifting under steam—how rift magmatism triggers methane venting from sedimentary basins. Geology 44, 767–770. https://doi.org/10.1130/G38049.1.

Blum, J.D., Sherman, L.S., Johnson, M.W., 2014. Mercury Isotopes in Earth and Environmental Sciences. Annu. Rev. Earth Planet. Sci. 42, 249–269. https://doi.org/10.1146/annurev-earth-050212-124107.

Bond, D.P.G., Wignall, P.B., 2014. Large igneous provinces and mass extinctions: an update. In: Volcanism, Impacts, and Mass Extinctions: Causes and Effects. Geological Society of America, pp. 29–55. https://doi.org/10.1130/2014.2505(02.

Bowen, G.J., Beerling, D.J., 2004. An integrated model for soil organic carbon and CO2 : implications for paleosol carbonate p CO2 paleobarometry. Glob. Biogeochem. Cycles 18. https://doi.org/10.1029/2003GB002117 n/a-n/a.

Bowen, G.J., Koch, P.L., Gingerich, P.D., Norris, R.D., Bains, S., Corfield, R.M., 2001. Refined isotope stratigraphy across the continental Paleocene-Eocene boundary on Polecat Bench in the Northern Bighorn Basin. In: Gingerich, P.D. (Ed.), Paleocene-Eocene Stratigraphy and Biotic Change in the Bighorn and Clarks Fork Basins, pp. 73–88. Wyoming.

Bowen, G.J., Clyde, W.C., Koch, P.L., Ting, S., Alroy, J., Tsubamoto, T., Wang, Yuanqing, Wang, Yuan, 2002. Mammalian dispersal at the paleocene/eocene boundary. Science 295 (80), 2062–2065. https://doi.org/10.1126/science.1068700.

Bowen, G.J., Beerling, D.J., Koch, P.L., Zachos, J.C., Quattlebaum, T., 2004. A humid climate state during the Palaeocene/Eocene thermal maximum. Nature 432, 495–499. https://doi.org/10.1038/nature03115.

Bowen, G.J., Maibauer, B.J., Kraus, M.J., Röhl, U., Westerhold, T., Steimke, A., Gingerich, P.D., Wing, S.L., Clyde, W.C., 2015. Two massive, rapid releases of carbon during the onset of the Palaeocene–Eocene thermal maximum. Nat. Geosci. 8, 44–47. https://doi.org/10.1038/ngeo2316.

Bower, J., Savage, K.S., Weinman, B., Barnett, M.O., Hamilton, W.P., Harper, W.F., 2008. Immobilization of mercury by pyrite (FeS2). Environ. Pollut. 156, 504–514. https://doi.org/10.1016/j.envpol.2008.01.011.

Bowman, K.L., Hammerschmidt, C.R., Lamborg, C.H., Swarr, G., 2015. Mercury in the North Atlantic Ocean: the U.S. GEOTRACES zonal and meridional sections. Deep-Sea Res. II Top. Stud. Oceanogr. 116, 251–261. https://doi.org/10.1016/j.dsr2.2014.07.004.

Burke, M.P., Hogue, T.S., Ferreira, M., Mendez, C.B., Navarro, B., Lopez, S., Jay, J.A., 2010. The effect of wildfire on soil mercury concentrations in southern California watersheds. Water Air Soil Pollut. 212, 369–385. https://doi.org/10.1007/s11270-010-0351-y.

Canudo, J., Keller, G., Molina, E., Ortiz, N., 1995. Planktic foraminiferal turnover and δ13C isotopes across the Paleocene-Eocene transition at Caravaca and Zumaya, Spain. Palaeogeogr. Palaeoclimatol. Palaeoecol. 114, 75–100. https://doi.org/10.1016/0031-0182(95)00073-U.

Cerling, T.E., 1984. The stable isotopic composition of modern soil carbonate and its relationship to climate. Earth Planet. Sci. Lett. 71, 229–240.

Charbonnier, G., Föllmi, K.B., 2017. Mercury enrichments in lower Aptian sediments support the link between Ontong Java large igneous province activity and oceanic anoxic episode 1a. Geology 45, 63–66. https://doi.org/10.1130/G38207.1.

Charbonnier, G., Morales, C., Duchamp-Alphonse, S., Westermann, S., Adatte, T., Föllmi, K.B., 2017. Mercury enrichment indicates volcanic triggering of Valanginian environmental change. Sci. Rep. 7, 40808. https://doi.org/10.1038/srep40808.

Chen, C., Guerit, L., Foreman, B.Z., Hassenruck-Gudipati, H.J., Adatte, T., Honegger, L., Perret, M., Sluijs, A., Castelltort, S., 2018. Estimating regional flood discharge during Palaeocene-Eocene global warming. Sci. Rep. 8, 1–8. https://doi.org/10.1038/s41598-018-31076-3.

Colombié, C., Lécuyer, C., Strasser, A., 2011. Carbon- and oxygen-isotope records of palaeoenvironmental and carbonate production changes in shallow-marine carbonates (Kimmeridgian, Swiss Jura). Geol. Mag. 148, 133–153. https://doi.org/10.1017/S0016756810000518.

Courtillot, V.E., Renne, P.R., 2003. On the ages of flood basalt events. Compt. Rendus Geosci. 335, 113–140. https://doi.org/10.1016/S1631-0713(03)00006-3.

Cramer, B.S., Wright, J.D., Kent, D.V., Aubry, M.P., 2003. Orbital climate forcing of δ13C excursions in the late Paleocene-early Eocene (chrons C24n-C25n). Paleoceanography 18, 1–25. https://doi.org/10.1029/2003PA000909.

Cui, Y., Kump, L.R., Ridgwell, A.J., Charles, A.J., Junium, C.K., Diefendorf, A.F., Freeman, K.H., Urban, N.M., Harding, I.C., 2011. Slow release of fossil carbon during the Palaeocene–Eocene Thermal Maximum. Nat. Geosci. 4, 481–485. https://doi.org/10.1038/ngeo1179.

DeConto, R.M., Galeotti, S., Pagani, M., Tracy, D., Schaefer, K., Zhang, T., Pollard, D., Beerling, D.J., 2012. Past extreme warming events linked to massive carbon release from thawing permafrost. Nature 484, 87–91. https://doi.org/10.1038/nature10929.

Dickens, G.R., O'Neil, J.R., Rea, D.K., Owen, R.M., 1995. Dissociation of oceanic methane hydrate as a cause of the carbon isotope excursion at the end of the Paleocene. Paleoceanography 10, 965–971.

Domingo, L., López-Martínez, N., Leng, M.J., Grimes, S.T., 2009. The Paleocene–Eocene Thermal Maximum record in the organic matter of the Claret and Tendruy continental sections (South-central Pyrenees, Lleida, Spain). Earth Planet. Sci. Lett. 281, 226–237. https://doi.org/10.1016/j.epsl.2009.02.025.

Dreyer, T., 1993. Quantified fluvial architecture in ephemeral stream deposits of the Esplugafreda Formation (Palaeocene), Tremp-Graus Basin, northern Spain. The Intern. ed. In: Alluvial Sedimentation. https://doi.org/10.1016/0037-0738(94)90117-1.

Duller, R.A., Armitage, J.J., Manners, H.R., Grimes, S., Jones, T.D., 2019. Delayed sedimentary response to abrupt climate change at the Paleocene-Eocene boundary, northern Spain. Geology 47, 159–162.

Dunkley Jones, T., Lunt, D.J., Schmidt, D.N., Ridgwell, A., Sluijs, A., Valdes, P.J., Maslin, M., 2013. Climate model and proxy data constraints on ocean warming across the Paleocene–Eocene Thermal Maximum. Earth Sci. Rev. 125, 123–145. https://doi.org/10.1016/j.earscirev.2013.07.004.

Dunkley Jones, T., Manners, H.R., Hoggett, M., Kirtland Turner, S., Westerhold, T., Leng, M.J., Pancost, R.D., Ridgwell, A., Alegret, L., Duller, R., Grimes, S.T., 2018. Dynamics of sediment flux to a bathyal continental margin section through the Paleocene–Eocene Thermal Maximum. Clim. Past 14, 1035–1049. https://doi.org/10.5194/cp-14-1035-2018.

Eldholm, O., Thomas, E., 1993. Environmental impact of volcanic margin formation. Earth Planet. Sci. Lett. 117, 319–329. https://doi.org/10.1016/0012-821X(93)90087-P.

Ericksen, J.A., Gustin, M.S., Schorran, D.E., Johnson, D.W., Lindberg, S.E., Coleman, J.S., 2003. Accumulation of atmospheric mercury in forest foliage. Atmos. Environ. 37, 1613–1622. https://doi.org/10.1016/S1352-2310(03)00008-6.

Ernst, R.E., 2014a. LIPs and environmental changes and catastrophes. In: Large Igneous Provinces. Cambridge University Press, Cambridge, pp. 418–458.

Ernst, R.E., 2014b. Links with carbonatites, kimberlites, and lamprophyres/lam. In: Large Igneous Provinces, pp. 245–276.

Fleck, J.A., Grigal, D.F., Nater, E.A., 1999. Mercury uptake by trees: an observational experiment. Water Air Soil Pollut. 115, 513–523. https://doi.org/10.1023/A:1005194608598.

Font, E., Adatte, T., Sial, A.N., Drude de Lacerda, L., Keller, G., Punekar, J., 2016. Mercury anomaly, Deccan volcanism, and the end-Cretaceous mass extinction. Geology 44, 171–174. https://doi.org/10.1130/G37451.1.

Frescholtz, T.F., Gustin, M.S., Schorran, D.E., Fernandez, G.C.J., 2003. Assessing the source of mercury in foliar tissue of quaking aspen. Environ. Toxicol. Chem. 22, 2114. https://doi.org/10.1897/1551-5028(2003)022<2114:ATSOMI>2.0.CO;2.

Frieling, J., Svensen, H.H., Planke, S., Cramwinckel, M.J., Selnes, H., Sluijs, A., 2016. Thermogenic methane release as a cause for the long duration of the PETM. Proc. Natl. Acad. Sci. 113, 12059–12064. https://doi.org/10.1073/pnas.1603348113.

Frieling, J., Gebhardt, H., Huber, M., Adekeye, O.A., Akande, S.O., Reichart, G.-J., Middelburg, J.J., Schouten, S., Sluijs, A., 2017. Extreme warmth and heat-stressed plankton in the tropics during the Paleocene-Eocene Thermal Maximum. Sci. Adv. 3 https://doi.org/10.1126/sciadv.1600891 e1600891.

Gehrke, G.E., Blum, J.D., Meyers, P.A., 2009. The geochemical behavior and isotopic composition of Hg in a mid-Pleistocene western Mediterranean sapropel. Geochim. Cosmochim. Acta 73, 1651–1665. https://doi.org/10.1016/j.gca.2008.12.012.

Godet, A., Durlet, C., Spangenberg, J.E., Föllmi, K.B., 2016. Estimating the impact of early diagenesis on isotope records in shallow-marine carbonates: a case study from the Urgonian platform in western Swiss Jura. Palaeogeogr. Palaeoclimatol. Palaeoecol. 454, 125–138. https://doi.org/10.4267/2042/61385.

Grasby, S.E., Sanei, H., Beauchamp, B., Chen, Z., 2013. Mercury deposition through the Permo–Triassic Biotic Crisis. Chem. Geol. 351, 209–216. https://doi.org/10.1016/j.chemgeo.2013.05.022.

Grasby, S.E., Beauchamp, B., Bond, D.P., Wignall, P.B., Sanei, H., 2016. Mercury anomalies associated with three extinction events (Capitanian Crisis, Latest Permian Extinction and the Smithian/Spathian Extinction) in NW Pangea. Geol. Mag. 153, 285–297. https://doi.org/10.1017/S0016756815000436.

Grasby, S.E., Shen, W., Yin, R., Gleason, J.D., Blum, J.D., Lepak, R.F., Hurley, J.P., Beauchamp, B., 2017. Isotopic signatures of mercury contamination in latest Permian oceans. Geology 45, 55–58. https://doi.org/10.1130/G38487.1.

Grasby, S.E., Them, T.R., Chen, Z., Yin, R., Ardakani, O.H., 2019. Mercury as a proxy for volcanic emissions in the geologic record. Earth Sci. Rev. 196, 102880. https://doi.org/10.1016/j.earscirev.2019.102880.

Gutjahr, M., Ridgwell, A., Sexton, P.F., Anagnostou, E., Pearson, P.N., Pälike, H., Norris, R.D., Thomas, E., Foster, G.L., 2017. Very large release of mostly volcanic carbon during the Palaeocene–Eocene Thermal Maximum. Nature 548, 573–577. https://doi.org/10.1038/nature23646.

Han, D.S., Orillano, M., Khodary, A., Duan, Y., Batchelor, B., Abdel-Wahab, A., 2014. Reactive iron sulfide (FeS)-supported ultrafiltration for removal of mercury (Hg(II)) from water. Water Res. 53, 310–321. https://doi.org/10.1016/j.watres.2014.01.033.

Haynes, L.L., Hönisch, B., 2020. The seawater carbon inventory at the Paleocene – Eocene Thermal Maximum. Proc. Natl. Acad. Sci. U. S. A. https://doi.org/10.1073/pnas.2003197117.

Heimdal, T.H., Callegaro, S., Svensen, H.H., Jones, M.T., Pereira, E., Planke, S., 2019. Evidence for magma–evaporite interactions during the emplacement of the Central Atlantic Magmatic Province (CAMP) in Brazil. Earth Planet. Sci. Lett. 506, 476–492. https://doi.org/10.1016/j.epsl.2018.11.018.

Higgins, J.A., Schrag, D.P., 2006. Beyond methane: towards a theory for the Paleocene–Eocene Thermal Maximum. Earth Planet. Sci. Lett. 245, 523–537. https://doi.org/10.1016/j.epsl.2006.03.009.

Holbrook, W.S., Larsen, H.C., Korenaga, J., Dahl-Jensen, T., Reid, I.D., Kelemen, P.B., Hopper, J.R., Kent, G.M., Lizarralde, D., Bernstein, S., Detrick, R.S., 2001. Mantle thermal structure and active upwelling during continental breakup in the North Atlantic. Earth Planet. Sci. Lett. 190, 251–266. https://doi.org/10.1016/S0012-821X(01)00392-2.

Honegger, L., Adatte, T., Spangenberg, J.E., Rugenstein, J.K.C., Poyatos-Moré, M., Puigdefàbregas, C., Chanvry, E., Clark, J., Fildani, A., Verrechia, E., Kouzmanov, K., Harlaux, M., Castelltort, S., 2019. Alluvial record of an early Eocene hyperthermal, Castissent Formation, Pyrenees, Spain. Clim. Past Discuss. 16, 227–243. https://doi.org/10.5194/cp-2019-88.

Immenhauser, A., Kenter, J.A.M., Ganssen, G., Bahamonde, J.R., Vliet, A.V.A.N., Saher, M.H., 2002. Origin and significance of isotope shifts in Pennsylvanian carbonates (Asturias, NW Spain). J. Sediment. Res. 72, 82–84.

Jin, H., Liebezeit, G., 2013. Distribution of total mercury in coastal sediments from Jade Bay and its catchment, Lower Saxony, Germany. J. Soils Sediments 13, 441–449. https://doi.org/10.1007/s11368-012-0626-6.

John, C.M., Bohaty, S.M., Zachos, J.C., Sluijs, A., Gibbs, S., Brinkhuis, H., Bralower, T.J., 2008. North American continental margin records of the Paleocene-Eocene thermal maximum: implications for global carbon and hydrological cycling. Paleoceanography 23, PA2217. https://doi.org/10.1029/2007PA001465.

Jolivet, M., Boulvais, P., 2020. Global significance of oxygen and carbon isotope compositions of pedogenic carbonates since the Cretaceous. Geosci. Front. 12, 101132. https://doi.org/10.1016/j.gsf.2020.12.012.

Jones, M.T., 2015. The environmental and climatic impacts of volcanic ash deposition. Volcanism Glob. Environ. Chang. 260–274. https://doi.org/10.1007/9781107415683.018.

Jones, D.S., Martini, A.M., Fike, D.A., Kaiho, K., 2017. A volcanic trigger for the late ordovician mass extinction? Mercury data from south China and laurentia. Geology 45, 631–634. https://doi.org/10.1130/G38940.1.

Jones, S.M., Hoggett, M., Greene, S.E., Dunkley Jones, T., 2019a. Large Igneous Province thermogenic greenhouse gas flux could have initiated Paleocene-Eocene Thermal Maximum climate change. Nat. Commun. 10, 5547. https://doi.org/10.1038/s41467-019-12957-1.

Jones, M.T., Percival, L.M.E., Stokke, E.W., Frieling, J., Mather, T.A., Riber, L., Schubert, B.A., Schultz, B., Tegner, C., Planke, S., Svensen, H.H., 2019b. Mercury anomalies across the Palaeocene-Eocene Thermal Maximum. Clim. Past 15, 217–236. https://doi.org/10.5194/cp-15-217-2019.

Kalvoda, J., Kumpan, T., Qie, W., Frýda, J., Bábek, O., 2019. Mercury spikes at the Devonian-Carboniferous boundary in the eastern part of the Rhenohercynian Zone (central Europe) and in the South China Block. Palaeogeogr. Palaeoclimatol. Palaeoecol. 531, 109221. https://doi.org/10.1016/j.palaeo.2019.05.043.

Keller, G., Mateo, P., Punekar, J., Khozyem, H., Gertsch, B., Spangenberg, J., Bitchong, A. M., Adatte, T., 2018. Environmental changes during the Cretaceous-Paleogene mass extinction and Paleocene-Eocene Thermal Maximum: implications for the Anthropocene. Gondwana Res. 56, 69–89. https://doi.org/10.1016/j.gr.2017.12.002.

Keller, G., Mateo, P., Monkenbusch, J., Thibault, N., Punekar, J., Spangenberg, J.E., Abramovich, S., Ashckenazi-Polivoda, S., Schoene, B., Eddy, M.P., Samperton, K.M., Khadri, S.F.R., Adatte, T., 2020. Mercury linked to Deccan Traps volcanism, climate change and the end-Cretaceous mass extinction. Glob. Planet. Chang. 194, 103312. https://doi.org/10.1016/j.gloplacha.2020.103312.

Kender, S., Bogus, K., Pedersen, G.K., Dybkjær, K., Mather, T.A., Mariani, E., Ridgwell, A., Riding, J.B., Wagner, T., Hesselbo, S.P., Leng, M.J., 2021. Paleocene/Eocene carbon feedbacks triggered by volcanic activity. Nat. Commun. 12, 5186. https://doi.org/10.1038/s41467-021-25536-0.

Kirtland Turner, S., 2018. Constraints on the onset duration of the Paleocene–Eocene Thermal Maximum. Philos. Trans. R. Soc. A Math. Phys. Eng. Sci. 376, 20170082. https://doi.org/10.1098/rsta.2017.0082.

Kirtland Turner, S., Ridgwell, A., 2013. Recovering the true size of an Eocene hyperthermal from the marine sedimentary record. Paleoceanography 28, 700–712. https://doi.org/10.1002/2013PA002541.

Kirtland Turner, S., Ridgwell, A., 2016. Development of a novel empirical framework for interpreting geological carbon isotope excursions, with implications for the rate of carbon injection across the PETM. Earth Planet. Sci. Lett. 435, 1–13. https://doi.org/10.1016/j.epsl.2015.11.027.

Kirtland Turner, S., Hull, P.M., Kump, L.R., Ridgwell, A., 2017. A probabilistic assessment of the rapidity of PETM onset. Nat. Commun. 8, 353. https://doi.org/10.1038/s41467-017-00292-2.

Klug, H.P., Alexander, L.E., 1974. X-Ray Diffraction Procedures: For Polycrystalline and Amorphous Materials, 2nd edition. John Wiley and Sons, Inc., New York.

Koch, P.L., Zachos, J.C., Gingerich, P.D., 1992. Correlation between isotope records in marine and continental carbon reservoirs near the Palaeocene/Eocene boundary. Nature 358, 319–322. https://doi.org/10.1038/358319a0.

Koch, P.L., Cruz, S., Zachos, J.C., Cruz, S., Dettman, D.L., 1995. Stable isotope stratigraphy and paleoclimatology of the Paleogene Bighorn Basin (Wyoming, USA). Palaeogeogr. Palaeoclimatol. Palaeoecol. 115, 61–89. https://doi.org/10.1016/0031-0182(94)00107-J.

Kongchum, M., Hudnall, W.H., Delaune, R.D., 2011. Relationship between sediment clay minerals and total mercury. J. Environ. Sci. Health A 46, 534–539. https://doi.org/10.1080/10934529.2011.551745.

Kübler, B., 1983. Cristallinité de l'illite, méthodes normalisées de préparations, méthodes normalisées de mesures. Série ADX Cah. Inst. Geol. Neuchâtel, Suisse, p. 1.

Kurtz, A.C., Kump, L.R., Arthur, M.A., Zachos, J.C., Paytan, A., 2003. Early Cenozoic decoupling of the global carbon and sulfur cycles. Paleoceanography 18, 1–14. https://doi.org/10.1029/2003PA000908.

Lamborg, C.H., Von Damm, K.L., Fitzgerald, W.F., Hammerschmidt, C.R., Zierenberg, R., 2006. Mercury and monomethylmercury in fluids from Sea Cliff submarine hydrothermal field, Gorda Ridge. Geophys. Res. Lett. 33, L17606. https://doi.org/10.1029/2006GL026321.

Leng, M.J., Marshall, J.D., 2004. Palaeoclimate interpretation of stable isotope data from lake sediment archives. Quat. Sci. Rev. 23, 811–831. https://doi.org/10.1016/j.quascirev.2003.06.012.

Li, J., Hu, X., Zachos, J.C., Garzanti, E., BouDagher-Fadel, M., 2020. Sea level, biotic and carbon-isotope response to the Paleocene–Eocene thermal maximum in Tibetan Himalayan platform carbonates. Glob. Planet. Chang. 194, 103316. https://doi.org/10.1016/j.gloplacha.2020.103316.

Li, J., Hu, X., Garzanti, E., Boudagher-fadel, M., 2021. Climate-driven hydrological change and carbonate platform demise induced by the Paleocene – Eocene Thermal Maximum (southern Pyrenees). Palaeogeogr. Palaeoclimatol. Palaeoecol. 567, 110250. https://doi.org/10.1016/j.palaeo.2021.110250.

Liu, Z., Horton, D.E., Tabor, C., Sageman, B.B., Percival, L.M.E., Gill, B.C., Selby, D., 2019. Assessing the contributions of comet impact and volcanism toward the climate perturbations of the Paleocene-Eocene Thermal Maximum. Geophys. Res. Lett. 46, 14798–14806. https://doi.org/10.1029/2019GL084818.

McCarren, H., Thomas, E., Hasegawa, T., Röhl, U., Zachos, J.C., 2008. Depth dependency of the Paleocene-Eocene carbon isotope excursion: Paired benthic and terrestrial biomarker records (Ocean Drilling Program Leg 208, Walvis Ridge). Geochem. Geophys. Geosyst. 9, Q10008. https://doi.org/10.1029/2008GC002116.

McInerney, F.A., Wing, S.L., 2011. The Paleocene-Eocene Thermal Maximum: a perturbation of carbon cycle, climate, and biosphere with implications for the future. Annu. Rev. Earth Planet. Sci. 39, 489–516. https://doi.org/10.1146/annurev-earth-040610-133431.

Minelli, N., Manzi, V., Roveri, M., 2013. The record of the Paleocene-Eocene thermal maximum in the Ager Basin (Central Pyrenees, Spain). Geol. Acta 11, 421–441. https://doi.org/10.1344/105.000002061.

Murphy, B.H., Farley, K.A., Zachos, J.C., 2010. An extraterrestrial 3He-based timescale for the Paleocene–Eocene thermal maximum (PETM) from Walvis Ridge, IODP Site 1266. Geochim. Cosmochim. Acta 74, 5098–5108. https://doi.org/10.1016/j.gca.2010.03.039.

Orue-Etxebarria, X., Pujalte, V., Bernaola, G., Apellaniz, E., Baceta, J., Payros, A., Nuñez-Betelu, K., Serra-Kiel, J., Tosquella, J., 2001. Did the Late Paleocene thermal maximum affect the evolution of larger foraminifers? Evidence from calcareous plankton of the Campo Section (Pyrenees, Spain). Mar. Micropaleontol. 41, 45–71. https://doi.org/10.1016/S0377-8398(00)00052-9.

Outridge, P.M., Sanei, H., Stern, G.A., Hamilton, P.B., Goodarzi, F., 2007. Evidence for control of mercury accumulation rates in Canadian High Arctic lake sediments by variations of aquatic primary productivity. Environ. Sci. Technol. 41, 5259–5265. https://doi.org/10.1021/es070408x.

Pagani, M., Huber, M., Sageman, B., 2014. Greenhouse climates. In: Treatise on Geochemistry. Elsevier, pp. 281–304. https://doi.org/10.1016/B978-0-08-095975-7.01314-0.

Patterson, W.P., Walter, L., 1994. Depletion of 13C in seawater ΣCO2 on modern carbonate platforms: significance for the carbon isotopic record of carbonates. Geology 22, 885–888.

Percival, L.M.E., Witt, M.L.I., Mather, T.A., Hermoso, M., Jenkyns, H.C., Hesselbo, S.P., Al-Suwaidi, A.H., Storm, M.S., Xu, W., Ruhl, M., 2015. Globally enhanced mercury deposition during the end-Pliensbachian extinction and Toarcian OAE: a link to the Karoo–Ferrar Large Igneous Province. Earth Planet. Sci. Lett. 428, 267–280. https://doi.org/10.1016/j.epsl.2015.06.064.

Percival, L.M.E., Ruhl, M., Hesselbo, S.P., Jenkyns, H.C., Mather, T.A., Whiteside, J.H., 2017. Mercury evidence for pulsed volcanism during the end-Triassic mass extinction. Proc. Natl. Acad. Sci. 114, 7929–7934. https://doi.org/10.1073/pnas.1705378114.

Percival, Lawrence M.E., Jenkyns, H.C., Mather, T.A., Dickson, A.J., Batenburg, S.J., Ruhl, M., Hesselbo, S.P., Barclay, R., Jarvis, I., Robinson, S.A., Woelders, L., 2018. Does large igneous province volcanism always perturb the mercury cycle? Comparing the records of Oceanic Anoxic Event 2 and the end-Cretaceous to other Mesozoic events. Am. J. Sci. 318, 799–860. https://doi.org/10.2475/08.2018.01.

Percival, L.M.E., Bergquist, B.A., Mather, T.A., Sanei, H., 2020. Sedimentary mercury enrichments as a tracer of large igneous province volcanism. In: Ernst, R.E., Dickson, A.J., Bekker, A. (Eds.), Large Igneous Provinces: A Driver of Global Environmental and Biotic Changes, pp. 247–262. https://doi.org/10.1002/9781119507444.ch11.

Plaziat, J., 1981. Late Cretaceous to late Eocene paleogeographic evolution of southwest Europe. Palaeogeogr. Palaeoclimatol. Palaeoecol. 36, 263–320.

Pujalte, V., Schmitz, B., Baceta, J.I., 2014. Sea-level changes across the Paleocene–Eocene interval in the Spanish Pyrenees, and their possible relationship with North Atlantic magmatism. Palaeogeogr. Palaeoclimatol. Palaeoecol. 393, 45–60. https://doi.org/10.1016/j.palaeo.2013.10.016.

Pujalte, V., Baceta, J.I., Schmitz, B., 2015. A massive input of coarse-grained siliciclastics in the Pyrenean Basin during the PETM: the missing ingredient in a coeval abrupt change in hydrological regime. Clim. Past 11, 1653–1672. https://doi.org/10.5194/cp-11-1653-2015.

Pyle, D.M., Mather, T.A., 2003. The importance of volcanic emissions for the global atmospheric mercury cycle. Atmos. Environ. 37, 5115–5124. https://doi.org/10.1016/j.atmosenv.2003.07.011.

Racki, G., 2020. Volcanism as a prime cause of mass extinctions: retrospectives and perspectives. In: Mass Extinctions, Volcanism, and Impacts: New Developments. Geological Society of America, pp. 1–34. https://doi.org/10.1130/2020.2544(01.

Racki, G., Rakociński, M., Marynowski, L., Wignall, P.B., 2018. Mercury enrichments and the Frasnian-Famennian biotic crisis: a volcanic trigger proved? Geology 46, 543–546. https://doi.org/10.1130/G40233.1.

Rampino, M.R., Stothers, R.B., 1988. Flood basalt volcanism during the past 250 million years. Science 241 (80), 663–668. https://doi.org/10.1126/science.241.4866.663.

Röhl, U., Westerhold, T., Bralower, T.J., Zachos, J.C., 2007. On the duration of the Paleocene-Eocene thermal maximum (PETM). Geochem. Geophys. Geosyst. 8, Q12002. https://doi.org/10.1029/2007GC001784.
Sanei, H., Grasby, S.E., Beauchamp, B., 2012. Latest Permian mercury anomalies. Geology 40, 63–66. https://doi.org/10.1130/G32596.1.
Saunders, A.D., 2016. Two LIPs and two Earth-system crises: the impact of the North Atlantic Igneous Province and the Siberian Traps on the Earth-surface carbon cycle. Geol. Mag. 153, 201–222. https://doi.org/10.1017/S0016756815000175.
Scaife, J.D., Ruhl, M., Dickson, A.J., Mather, T.A., Jenkyns, H.C., Percival, L.M.E., Hesselbo, S.P., Cartwright, J., Eldrett, J.S., Bergman, S.C., Minisini, D., 2017. Sedimentary mercury enrichments as a marker for submarine large igneous province volcanism? Evidence from the mid-Cenomanian event and oceanic anoxic event 2 (Late Cretaceous). Geochem. Geophys. Geosyst. 18, 4253–4275. https://doi.org/10.1002/2017GC007153.
Schmitz, B., Pujalte, V., 2003. Sea-level, humidity, and land-erosion records across the initial Eocene thermal maximum from a continental-marine transect in northern Spain. Geology 31, 689. https://doi.org/10.1130/G19527.1.
Schmitz, B., Pujalte, V., 2007. Abrupt increase in seasonal extreme precipitation at the Paleocene-Eocene boundary. Geology 35, 215. https://doi.org/10.1130/G23261A.1.
Schmitz, B., Asaro, F., Molina, E., Monechi, S., von Salis, K., Speijer, R.P., 1997. High-resolution iridium, δ13C, δ18O, foraminifera and nannofossil profiles across the latest Paleocene benthic extinction event at Zumaya, Spain. Palaeogeogr. Palaeoclimatol. Palaeoecol. 133, 49–68. https://doi.org/10.1016/S0031-0182(97)00024-2.
Schroeder, W.H., Munthe, J., 1998. Atmospheric mercury—an overview. Atmos. Environ. 32, 809–822. https://doi.org/10.1016/S1352-2310(97)00293-8.
Schuster, P.F., Schaefer, K.M., Aiken, G.R., Antweiler, R.C., Dewild, J.F., Gryziec, J.D., Gusmeroli, A., Hugelius, G., Jafarov, E., Krabbenhoft, D.P., Liu, L., Herman-Mercer, N., Mu, C., Roth, D.A., Schaefer, T., Striegl, R.G., Wickland, K.P., Zhang, T., 2018. Permafrost stores a globally significant amount of mercury. Geophys. Res. Lett. 45, 1463–1471. https://doi.org/10.1002/2017GL075571.
Secord, R., Gingerich, P.D., Lohmann, K.C., MacLeod, K.G., 2010. Continental warming preceding the Palaeocene–Eocene thermal maximum. Nature 467, 955–958. https://doi.org/10.1038/nature09441.
Self-Trail, J.M., Powars, D.S., Watkins, D.K., Wandless, G.A., 2012. Calcareous nannofossil assemblage changes across the Paleocene–Eocene Thermal Maximum: evidence from a shelf setting. Mar. Micropaleontol. 92–93, 61–80. https://doi.org/10.1016/j.marmicro.2012.05.003.
Self-Trail, J.M., Robinson, M.M., Bralower, T.J., Sessa, J.A., Hajek, E.A., Kump, L.R., Trampush, S.M., Willard, D.A., Edwards, L.E., Powars, D.S., Wandless, G.A., 2017. Shallow marine response to global climate change during the Paleocene-Eocene Thermal Maximum, Salisbury Embayment, USA. Paleoceanography 32, 710–728. https://doi.org/10.1002/2017PA003096.
Sheldon, N.D., Tabor, N.J., 2009. Quantitative paleoenvironmental and paleoclimatic reconstruction using paleosols. Earth Sci. Rev. 95, 1–52. https://doi.org/10.1016/j.earscirev.2009.03.004.
Shen, J., Algeo, T.J., Chen, J., Planavsky, N.J., Feng, Q., Yu, J., Liu, J., 2019a. Mercury in marine Ordovician/Silurian boundary sections of South China is sulfide-hosted and non-volcanic in origin. Earth Planet. Sci. Lett. 511, 130–140. https://doi.org/10.1016/j.epsl.2019.01.028.
Shen, J., Chen, J., Algeo, T.J., Yuan, S., Feng, Q., Yu, J., Zhou, L., O'Connell, B., Planavsky, N.J., 2019b. Evidence for a prolonged Permian–Triassic extinction interval from global marine mercury records. Nat. Commun. 10, 1563. https://doi.org/10.1038/s41467-019-09620-0.
Shen, J., Yin, R., Zhang, S., Algeo, T.J., Bottjer, D.J., Yu, J., Xu, G., Penman, D., Wang, Y., Li, L., Shi, X., Planavsky, N.J., Feng, Q., Xie, S., 2022. Intensified continental chemical weathering and carbon-cycle perturbations linked to volcanism during the Triassic–Jurassic transition. Nature Communications 13 (1), 299. https://doi.org/10.1038/s41467-022-27965-x.
Shen, J., Yu, J., Chen, J., Algeo, T.J., Xu, G., Feng, Q., Shi, X., Planavsky, N.J., Shu, W., Xie, S., 2019c. Mercury evidence of intense volcanic effects on land during the Permian-Triassic transition. Geology 47, 1117–1121. https://doi.org/10.1130/G46679.1.
Shen, J., Feng, Q., Algeo, T.J., Liu, Jinling, Zhou, C., Wei, W., Liu, Jiangsi, Them, T.R., Gill, B.C., Chen, J., 2020. Sedimentary host phases of mercury (Hg) and implications for use of Hg as a volcanic proxy. Earth Planet. Sci. Lett. 543, 116333. https://doi.org/10.1016/j.epsl.2020.116333.
Sial, A.N., Lacerda, L.D., Ferreira, V.P., Frei, R., Marquillas, R.A., Barbosa, J.A., Gaucher, C., Windmöller, C.C., Pereira, N.S., 2013. Mercury as a proxy for volcanic activity during extreme environmental turnover: the Cretaceous–Paleogene transition. Palaeogeogr. Palaeoclimatol. Palaeoecol. 387, 153–164. https://doi.org/10.1016/j.palaeo.2013.07.019.
Sial, A.N., Chen, J., Lacerda, L.D., Frei, R., Tewari, V.C., Pandit, M.K., Gaucher, C., Ferreira, V.P., Cirilli, S., Peralta, S., Korte, C., Barbosa, J.A., Pereira, N.S., 2016. Mercury enrichment and Hg isotopes in Cretaceous–Paleogene boundary successions: links to volcanism and palaeoenvironmental impacts. Cretac. Res. 66, 60–81. https://doi.org/10.1016/j.cretres.2016.05.006.
Slemr, F., Schuster, G., Seiler, W., 1985. Distribution, speciation, and budget of atmospheric mercury. J. Atmos. Chem. 3, 407–434. https://doi.org/10.1007/BF00053870.
Sluijs, A., Schouten, S., Pagani, M., Woltering, M., Brinkhuis, H., Sinninghe Damsté, J.S., Dickens, G.R., Huber, M., Reichart, G.-J., Stein, R., Matthiessen, J., Lourens, L.J., Pedentchouk, N., Backman, J., Moran, K., the Expedition, S, 2006. Subtropical Arctic Ocean temperatures during the Palaeocene/Eocene Thermal Maximum. Nature 441, 610–613. https://doi.org/10.1038/nature04668.
Sluijs, A., Brinkhuis, H., Schouten, S., Bohaty, S.M., John, C.M., Zachos, J.C., Reichart, G.-J., Sinninghe Damsté, J.S., Crouch, E.M., Dickens, G.R., 2007. Environmental precursors to rapid light carbon injection at the Palaeocene/Eocene boundary. Nature 450, 1218–1221. https://doi.org/10.1038/nature06400.
Sluijs, A., Bijl, P.K., Schouten, S., Röhl, U., Reichart, G.J., Brinkhuis, H., 2011. Southern ocean warming, sea level and hydrological change during the Paleocene-Eocene thermal maximum. Clim. Past 7, 47–61. https://doi.org/10.5194/cp-7-47-2011.
Stap, L., Sluijs, A., Thomas, E., Lourens, L., 2009. Patterns and magnitude of deep sea carbonate dissolution during Eocene Thermal Maximum 2 and H2, Walvis Ridge, southeastern Atlantic Ocean. Paleoceanography 24, 1–13. https://doi.org/10.1029/2008PA001655.
Stassen, P., 2016. Global warming then and now. Nat. Geosci. 9, 268–269. https://doi.org/10.1038/ngeo2691.
Stassen, P., Dupuis, C., Morsi, A.M., Steurbaut, E., Speijer, R.P., 2009. Reconstruction of a latest Paleocene shallow-marine eutrophic paleoenvironment at Sidi Nasseur (Central Tunisia) based on foraminifera, ostracoda, calcareous nannofossils and stable isotopes (δ13C, δ18O). Geol. Acta 7, 93–112. https://doi.org/10.1344/105.000000273.
Stern, G.A., Sanei, H., Roach, P., DeLaronde, J., Outridge, P.M., 2009. Historical interrelated variations of mercury and aquatic organic matter in lake sediment cores from a subarctic lake in Yukon, Canada: further evidence toward the algal-mercury scavenging hypothesis. Environ. Sci. Technol. 43, 7684–7690. https://doi.org/10.1021/es902186s.
Storey, M., Duncan, R.A., Swisher, C.C., 2007a. Paleocene-Eocene Thermal Maximum and the opening of the Northeast Atlantic. Science 316 (80), 587–589. https://doi.org/10.1126/science.1135274.
Storey, M., Duncan, R.A., Tegner, C., 2007b. Timing and duration of volcanism in the North Atlantic Igneous Province: implications for geodynamics and links to the Iceland hotspot. Chem. Geol. 241, 264–281. https://doi.org/10.1016/j.chemgeo.2007.01.016.
Storme, J.-Y., Devleeschouwer, X., Schnyder, J., Cambier, G., Baceta, J.I., Pujalte, V., Di Matteo, A., Iacumin, P., Yans, J., 2012. The Palaeocene/Eocene boundary section at Zumaia (Basque-Cantabric Basin) revisited: new insights from high-resolution magnetic susceptibility and carbon isotope chemostratigraphy on organic matter (δ13Corg). Terra Nova 24, 310–317. https://doi.org/10.1111/j.1365-3121.2012.01064.x.
Svensen, H., Planke, S., Malthe-Sørenssen, A., Jamtveit, B., Myklebust, R., Rasmussen Eidem, T., Rey, S.S., 2004. Release of methane from a volcanic basin as a mechanism for initial Eocene global warming. Nature 429, 542–545. https://doi.org/10.1038/nature02566.
Svensen, H., Planke, S., Corfu, F., 2010. Zircon dating ties NE Atlantic sill emplacement to initial Eocene global warming. J. Geol. Soc. Lond. 167, 433–436. https://doi.org/10.1144/0016-76492009-125.
Swart, P.K., 2008. Global synchronous changes in the carbon isotopic composition of carbonate sediments unrelated to changes in the global carbon cycle. Proc. Natl. Acad. Sci. 105, 13741–13745. https://doi.org/10.1073/pnas.0802841105.
Them, T.R., Jagoe, C.H., Caruthers, A.H., Gill, B.C., Grasby, S.E., Gröcke, D.R., Yin, R., Owens, J.D., 2019. Terrestrial sources as the primary delivery mechanism of mercury to the oceans across the Toarcian Oceanic Anoxic Event (Early Jurassic). Earth Planet. Sci. Lett. 507, 62–72. https://doi.org/10.1016/j.epsl.2018.11.029.
Thibodeau, A.M., Bergquist, B.A., 2017. Do mercury isotopes record the signature of massive volcanism in marine sedimentary records? Geology 45, 95–96. https://doi.org/10.1130/focus012017.1.
Thibodeau, A.M., Ritterbush, K., Yager, J.A., West, A.J., Ibarra, Y., Bottjer, D.J., Berelson, W.M., Bergquist, B.A., Corsetti, F.A., 2016. Mercury anomalies and the timing of biotic recovery following the end-Triassic mass extinction. Nat. Commun. 7, 11147. https://doi.org/10.1038/ncomms11147.
Thomas, D.J., Bralower, T.J., 2005. Sedimentary trace element constraints on the role of North Atlantic Igneous Province volcanism in late Paleocene-early Eocene environmental change. Mar. Geol. 217, 233–254. https://doi.org/10.1016/j.margeo.2005.02.009.
Westerhold, T., Röhl, U., McCarren, H.K., Zachos, J.C., 2009. Latest on the absolute age of the Paleocene–Eocene Thermal Maximum (PETM): new insights from exact stratigraphic position of key ash layers +19 and −17. Earth Planet. Sci. Lett. 287, 412–419. https://doi.org/10.1016/j.epsl.2009.08.027.
Wieczorek, R., Fantle, M.S., Kump, L.R., Ravizza, G., 2013. Geochemical evidence for volcanic activity prior to and enhanced terrestrial weathering during the Paleocene Eocene Thermal Maximum. Geochim. Cosmochim. Acta 119, 391–410. https://doi.org/10.1016/j.gca.2013.06.005.
Wignall, P., 2005. The link between large and mass extinctions. Elements 1, 293–297.
Wilkinson, C.M., Ganerød, M., Hendriks, B.W.H., Eide, E.A., 2017. Compilation and appraisal of geochronological data from the North Atlantic Igneous Province (NAIP). Geol. Soc. Lond. Spec. Publ. 447, 69–103. https://doi.org/10.1144/SP447.10.
Wotzlaw, J.-F., Bindeman, I.N., Schaltegger, U., Brooks, C.K., Naslund, H.R., 2012. High-resolution insights into episodes of crystallization, hydrothermal alteration and remelting in the Skaergaard intrusive complex. Earth Planet. Sci. Lett. 355–356, 199–212. https://doi.org/10.1016/j.epsl.2012.08.043.
Zachos, J.C., Wara, M.W., Bohaty, S., Delaney, M.L., Petrizzo, M.R., Brill, A., Bralower, T.J., Premoli-Silva, I., 2003. A transient rise in tropical sea surface temperature during the Paleocene-Eocene Thermal Maximum. Science 302 (80), 1551–1554. https://doi.org/10.1126/science.1090110.
Zachos, J.C., Röhl, U., Schellenberg, S.A., Sluijs, A., Hodell, D.A., Kelly, D.C., Thomas, E., Nicolo, M., Raffi, I., Lourens, L.J., McCarren, H., Kroon, D., 2005. Rapid acidification of the ocean during the Paleocene-Eocene thermal maximum. Science 308, 1611–1615. https://doi.org/10.1126/science.1109004.

Zachos, J.C., Dickens, G.R., Zeebe, R.E., 2008. An early Cenozoic perspective on greenhouse warming and carbon-cycle dynamics. Nature 451, 279–283. https://doi.org/10.1038/nature06588.

Zamagni, J., Mutti, M., Ballato, P., Kosir, A., 2012. The Paleocene-Eocene thermal maximum (PETM) in shallow-marine successions of the Adriatic carbonate platform (SW Slovenia). Geol. Soc. Am. Bull. 124, 1071–1086. https://doi.org/10.1130/B30553.1.

Zeebe, R.E., Zachos, J.C., Dickens, G.R., 2009. Carbon dioxide forcing alone insufficient to explain Palaeocene–Eocene Thermal Maximum warming. Nat. Geosci. 2, 576–580. https://doi.org/10.1038/ngeo578.

Zeebe, R.E., Dickens, G.R., Ridgwell, A., Sluijs, A., Thomas, E., 2014. Onset of carbon isotope excursion at the Paleocene-Eocene thermal maximum took millennia, not 13 years. Proc. Natl. Acad. Sci. 111, E1062–E1063. https://doi.org/10.1073/pnas.1321177111.

Zeebe, R.E., Ridgwell, A., Zachos, J.C., 2016. Anthropogenic carbon release rate unprecedented during the past 66 million years. Nat. Geosci. 9, 325–329. https://doi.org/10.1038/ngeo2681.

Zhang, Q., Ding, L., Kitajima, K., Valley, J.W., Zhang, B., Xu, X., Willems, H., Klügel, A., 2020. Constraining the magnitude of the carbon isotope excursion during the Paleocene-Eocene thermal maximum using larger benthic foraminifera. Glob. Planet. Chang. 184, 103049. https://doi.org/10.1016/j.gloplacha.2019.103049.

Zintwana, M.P., Cawthorn, R.G., Ashwal, L.D., Roelofse, F., Cronwright, H., 2012. Mercury in the Bushveld complex, South Africa, and the Skaergaard intrusion, Greenland. Chem. Geol. 320–321, 147–155. https://doi.org/10.1016/j.chemgeo.2012.06.001.